Modelling and Identification for Control of Gas Bearings

Theisen, Lukas Roy Svane; Niemann, Hans Henrik; Santos, Ilmar; Galeazzi, Roberto; Blanke, Mogens

Published in:
Mechanical Systems and Signal Processing

Link to article, DOI:
10.1016/j.ymssp.2015.09.016

Publication date:
2015

Document Version
Peer reviewed version

Modelling and Identification for Control of Gas Bearings

Lukas R. S. Theisen[1], Hans H. Niemann[1], Ilmar F. Santos[2], Roberto Galeazzi[1], Mogens Blanke[1,3]

[1]*Dept. of Electrical Engineering and* [2]*Dept. of Mechanical Engineering*
Technical University of Denmark, DK 2800 Kgs. Lyngby, Denmark
[3]*AMOS CoE, Institute for Technical Cybernetics*
Norwegian University of Science and Technology, NO 7491 Trondheim, Norway
Email: {lrst,hhn,mb,rg}@elektro.dtu.dk, ifs@mek.dtu.dk

Abstract

Gas bearings are popular for their high speed capabilities, low friction and clean operation, but suffer from poor damping, which poses challenges for safe operation in presence of disturbances. Enhanced damping can be achieved through active lubrication techniques using feedback control laws. Such control design requires models with low complexity, able to describe the dominant dynamics from actuator input to sensor output over the relevant range of operation. The mathematical models based on first principles are not easy to obtain, and in many cases, they cannot be directly used for control design due to their complexity and parameter uncertainties. As an alternative, this paper presents an experimental technique for "in situ" identification of low complexity models of the entire rotor-bearing-actuator system. Using grey-box identification techniques, the approach is shown to be easily applied to industrial rotating machinery with gas bearings and to allow for subsequent control design. The paper shows how piezoelectric actuators in a gas bearing are efficiently used to perturb the gas film for identification over relevant ranges of rotational speed and gas injection pressure. Parameter-varying linear models are found to capture the dominant dynamics of the system over the range of operation. Based on the identified models, decentralised proportional control is designed and is shown to obtain the required damping in theory as well as in a laboratory test rig.

Keywords:
Active Gas Bearings, Experimental Techniques, Grey-Box Modelling, Rotordynamics, System Identification

1. Introduction

Passive and active gas bearings are receiving growing attention for their high speed operation capabilities. While passive gas bearings offer advantages of high speed operation, low friction, and clean and abundant air as lubricant, they suffer from low damping and vibration instabilities [1, 2, 3]. The damping and stability properties can be improved by two methods. One is through foil bearings [4, 5, 6] that exploit friction between bumps and foil. Such solutions are relatively cheap, but friction is a significant design challenge [7]. An alternative is to use a mechatronic approach in the form of active control of the gas bearing using piezo actuation [8] or active inherent restrictors [9]. The controllers for such systems could be tuned experimentally, with the uncertainty and lack of quality assurance this method implies, or they could be stringently designed based on dynamic models with documentable performance properties. The latter requires a suitable model, which in a simple manner describes the relation from actuator input to measured output, representing the dynamics of the journal in the frequency range where control is needed. Concerning modelling, air-injection actuators have only received sparse attention. In contrast, electromagnetical actuators and oil bearings have been well covered. Modelling and a linear parameter varying control design were presented for a rotor supported by an oil bearing and an electromagnetically actuated bearing in [10], which showed ability to reduce vibrations and to allow rub-free crossing of the first resonance frequency. Current state of the art models of controllable gas bearings rely on solving the modified Reynolds equation [3], which emerges from including the external controllable lubricant injection into the Reynolds equation. No general closed analytical solutions exist for the equation considering bearings with finite dimension. Solutions are therefore found iteratively over time, and the input-output relationship between piezoactuator and rotor lateral displacement is not easily derived. Literature has

therefore generally presented experimentally tuned controllers, e.g. in [8]. Some authors have proposed on-off control rules [11], where the opening of the valves changed the journal pressure, which in turn changed the critical speeds, allowing the rotor to cross them safely. Such approach, however, does not improve the damping characteristics of the gas bearing.

Models suitable for controller design can be developed using system identification. Such models can have low complexity and can yet provide a convenient basis for synthesising controllers [12]. Such models can leave out the details and high order associated with mechanical models based on first principles. Only few results exist for controllable gas bearings, whereas the literature is rich on active magnetic bearings (AMB). AMBs have inherently unstable dynamics [13, 14, 15] and therefore require stabilising controllers. For the non-rotating case, the horizontal and vertical AMB dynamics are uncoupled, therefore a model is developed for each of the two directions. In [16] and [14], a frequency based identification approach was used to develop black-box models of a rotor supported by AMBs. This allowed development of high order continuous time models for a non-rotating shaft supported by AMBs, which sufficed for controller design. In [17], a frequency based method was proposed for identification of the transfer function matrix model of a non-rotating shaft supported by AMBs. The method consisted of steps identifying the submodels separately and finally combining them together. In [13], a similar approach was proposed and deliberately poor controllers were used to allow identification of the poles on the real axis, which are in general not easily identified. In [18], a predictor-based subspace identification algorithm was proposed to identify the dynamics of a non-rotating AMB system, and the obtained model was used to design robust controllers. In [19] a simple black-box model was proposed to represent the vertical displacement of a simple non-rotating rigid shaft supported by AMBs, where the model parameters were estimated online. In [20], an iterative frequency based joint identification/controller design scheme for a non-rotating shaft supported by AMBs was applied using an LQ criterion.

Controllable gas bearings differ from AMBs in the sense that gas bearings can be designed to be open loop stable, hence open loop identification schemes can be used. The lateral dynamics is though coupled due to aerostatic effects even in the non-rotating case. Recent work [21] showed that grey-box system identification could be a means to develop such models. The main contribution of this work relies on: a) grey-box identification to develop low complexity models of the entire rotor-bearing-actuator system and b) extension of the early results from [21] by investigating the system dynamics as function of both gas injection pressure and rotational speed, which are the two main variables that influence system dynamic behaviour when the static load and the bearing geometry are kept constant [22]. The earlier models from [21] need to be extended to include the dynamics of the piezoelectric actuators and to capture the delay between the displacement of the piezoelectric actuator and the pressure build-up in the journal. The experimental procedure is developed aiming at industrial applications to complex rotating systems supported by gas bearings, where first principles modelling is rarely simple and accurate enough for controller design.

The paper is structured as follows: a brief overview of the experimental test rig is given in Sec. 2. The piezoelectric actuators are then characterised. The static gain from piezoactuator position to disc position is experimentally characterised. Section 3 presents an experimentally-based model of the rotor-bearing system obtained for a set of operational conditions through grey-box identification techniques. Regression techniques are used in Sec. 4 to fit polynomial surfaces to experimental data and build a linear parameter varying model of the entire controllable rotor-bearing system, which captures the essential behaviour across the operational range. Section 5 presents the design of a decentralised proportional controller to confirm the suitability of the identified models for controller design and the results are experimentally verified. Sections 6 and 7 evaluate critically the results, showing that the controller enhances the damping properties of the gas bearing as expected.

Notation

The paper uses upper case bold letters for matrices $\mathbf{A}$, lower case bold letters for vectors $\mathbf{a}$ and non-bold letters for scalars a or A. When relevant, clear distinctions are made to address time signals $a(t)$ and the Laplace transformed $a(s)$. Units for rotational speeds are listed in revolutions per minute ($1rpm = 1/60Hz$), and pressures are listed in bar ($1bar = 100,000Pa$).

Test rig dimension	Bearing length [mm]	Bearing diameter [mm]	Shaft length [mm]	Shaft mass [kg]	Disc diameter [mm]	Disc mass [kg]	Orifice diameter [mm]
Value	40	40	500	2.04	140	1.5	2

Table 1: Controllable gas bearing test rig parameters.

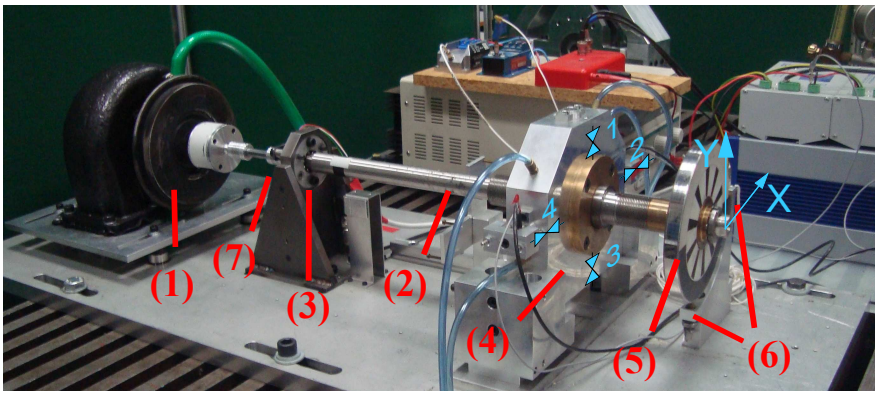

Figure 1: The experimental controllable gas bearing setup. A turbine (1) drives a flexible shaft (2), which is supported by both a ball bearing (3) and the controllable gas bearing (4) with four piezoactuated injectors. A disc (5) is mounted in one end to preload the journal and displacement sensors (6) measure the lateral movement of the disc in the shown reference frame. A quadrature encoder (7) measures the angular position.

2. Experimental Setup of Controllable Gas Bearing Test Rig

The experimental controllable gas bearing setup at hand is shown in Fig. 1. It consists of a turbine (1) driving a flexible shaft (2) supported by both a ball bearing (3) and the controllable gas bearing (4), in which pressurised air is injected through four piezoactuated injectors numbered as shown. The injection pressure P_{inj} is measured by a mechanical gauge before splitting up to the four piezoactuators. A disc (5) is mounted in one end to pre-load the journal. The horizontal and vertical disc movement $\mathbf{p} \triangleq [p_x, p_y]^{\mathrm{T}}$ is measured at the disc location using eddy current sensors (6) in the coordinate frame specified in the figure. The angular position of the rotor ϕ is measured by an optical quadrature encoder (7). The position of the i-th piezoactuator can be controlled through a voltage input $u_{p,i} \in [0; 10]V$, where an increasing voltage expands the piezostacks by up to 45 μm, which closes the injector. Figure 2 shows a CAD drawing of the test rig, where the gas bearing is cut in half to visualise the control mechanism. The nominal clearance of the gas bearing is 25 μm. Given the right conditions of sufficient injection pressure and sufficiently low rotational speed, the gas film generates restoring forces and thereby keeps the rotor levitating about a stable equilibrium, and opening or closing an injector perturbs the gas film. Physical dimensions of the test rig are shown in Table 1. All measurements are sampled with period $T_s = 0.2\ ms$. A detailed description of the setup is available in [23].

The piezoelectric stacks in the piezoactuators have two inherent nonlinear phenomena [24, 25]: creep and hysteresis. Hysteresis causes uncertainties in the piezoactuator position, which is a challenge for modelling and control. To counteract these nonlinear effects, decentralised PD-controllers are deployed. The controllers allow piezoactuator i, $i \in \{1, 2, 3, 4\}$ to track a reference position $r_{p,i}$. This is described in detail in Appendix A, and it is shown, that the closed loop piezoactuator dynamics can be captured by linear models, which is pursued further in Sec. 3.7.

The four piezoactuators are available to control the shaft displacement in x and y. Individual control of the piezoactuators gives the challenge of control allocation. Instead they are pairwise controlled using a differential principle. Piezoactuator reference positions $\mathbf{r}(t) \triangleq [r_x(t), r_y(t)]^{\mathrm{T}}$ are commanded using:

$$\begin{aligned} r_{p,1}(t) &= r_0 + r_y(t) & \qquad r_{p,2}(t) &= r_0 + r_x(t), \\ r_{p,3}(t) &= r_0 - r_y(t) & \qquad r_{p,4}(t) &= r_0 - r_x(t), \end{aligned} \tag{1}$$

i.e. one reference signal r_x is sent to the pair of piezoactuators mounted horizontally, and one reference signal r_y is sent to the pair mounted vertically as shown in Fig. 3. The constant offset r_0 is chosen to ensure the largest dynamical

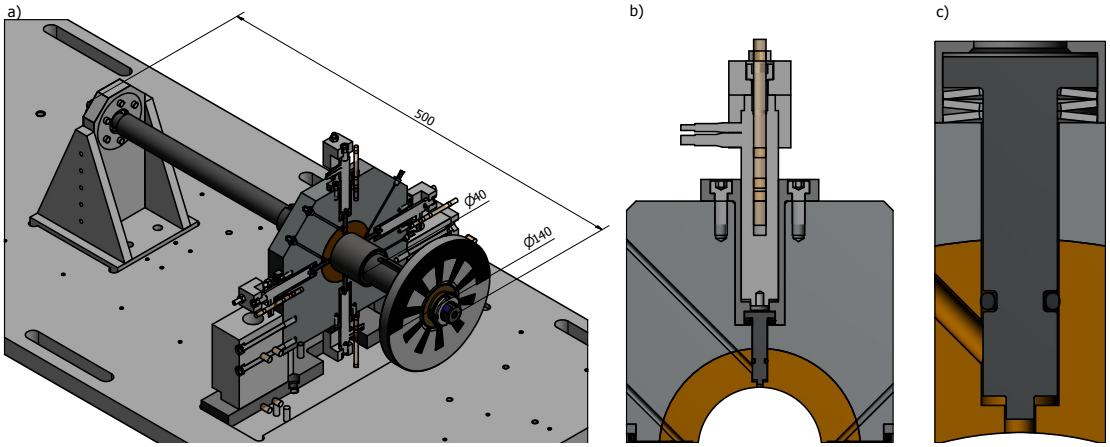

Figure 2: CAD drawing of the test rig: a) the test rig with the controllable gas bearing cut in half. Major dimensions are included in millimetre [*mm*]. b) zoom of a piezoactuator. The piezo electric stack pushes a pin, which controls the injector opening. c) zoom of the injector pin and journal.

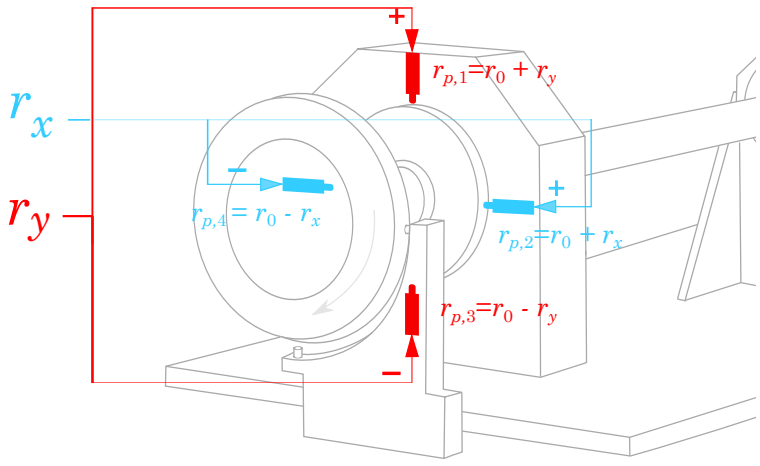

Figure 3: The piezoactuators are controlled pairwise using a differential principle. A reference signal r_x is sent to the pair of piezoactuators mounted horizontally, and a reference signal r_y is sent to the pair mounted vertically.

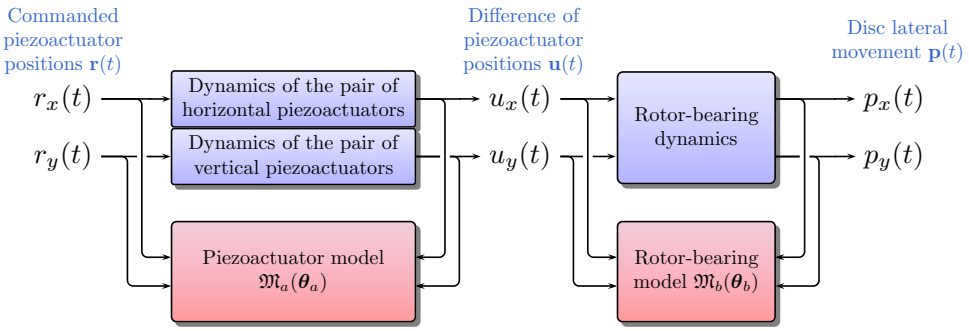

Figure 4: Overview of the system identification process. A perturbation of the commanded piezoactuator positions perturbs both the piezoactuators and the shaft and disc. An actuator model can the be identified from the $\{\mathbf{r}, \mathbf{u}\}$ data sets, and a rotor-bearing model from the $\{\mathbf{u}, \mathbf{p}\}$ data sets.

range avoiding actuator saturation. The individual piezoactuator positions are similarly mapped to a vector containing the difference of piezoactuator positions $\mathbf{u}(t)$:

$$\mathbf{u}(t) \triangleq [u_x(t), u_y(t)]^{\mathrm{T}} = [y_{p,2}(t) - y_{p,4}(t), y_{p,1}(t) - y_{p,3}(t)]^{\mathrm{T}} \tag{2}$$

The measurements of this difference of piezoactuator positions combined with the measurement of lateral disc movement allows modelling of actuator and bearing dynamics as individual linear subsystems. A rotor-bearing model is set up to describe the dynamics from piezoactuator position to lateral disc movement $[p_x, p_y]^{\mathrm{T}}$. An actuator model is set up to describe the relation from commanded piezoactuator positions $[r_x, r_y]^{\mathrm{T}}$ to piezoactuator position $[u_x, u_y]^{\mathrm{T}}$. The measured inputs and outputs of each subsystem are used to identify models as shown in Fig. 4. The entire rotor-bearing-actuator model $\mathbf{G}$ is then obtained as the interconnection of the rotor-bearing model $\mathbf{G}_{rb}$ and the actuator model $\mathbf{G}_{act}$:

$$\mathbf{G} = \mathbf{G}_{rb}\mathbf{G}_{act} \tag{3}$$

The individual models are derived in the following sections.

3. Experimentally-Based Modelling Aided by Grey-Box Identification

This section presents a low-complexity linear dynamical model describing the controllable gas bearing and rotor dynamics. The proposed model is shown to capture the dominant dynamics well, and its simplicity makes it suitable for controller design. The model parameters are found from experimental data using grey-box system identification [26]. Experiments performed over the operating range allow the description of the overall dynamic behaviour of the controllable gas bearing. Multiple data sets collected at each operational condition are used for cross-validation ensuring the quality of the identified models.

3.1. Static Input-Output Gain Modelling of Rotor-Bearing

The presence of nonlinear phenomena in the shaft actuation is assessed by the collection of a staircase response, where a stepwise increasing voltage is applied to the commanded piezoactuator positions $\mathbf{r}$, followed by a stepwise decreasing voltage. The response allows the generation of a steady state gain mapping showing shaft equilibrium position $\mathbf{p}$ as a function of the difference of piezoactuator positions $\mathbf{u}$. Figure 5 shows such a mapping for the injection pressure $\bar{P}_{\mathrm{inj}} = 6\ bar$, and the rotational speed $\bar{\Omega} = 0\ rpm$. The linear relation from inputs to outputs is evident. Cross-coupling gains from the aerostatic effect are also present in the system, though with small influence. This analysis shows no evidence of hysteresis or other nonlinear phenomena affecting the shaft position. Similar results are obtained for other injection pressures and rotation speeds, though with varying slopes and equilibrium position. The error in equilibrium position from approximating the static gain linear is less than 0.95 μm over the range of applied inputs with root mean square errors $[\sigma_{g0,xx}, \sigma_{g0,xy}, \sigma_{g0,yx}, \sigma_{g0,yy}]^{\mathrm{T}} = [0.44, 0.037, 0.059, 0.21]^{\mathrm{T}} \mu m$. Therefore linearity is a reasonable approximation.

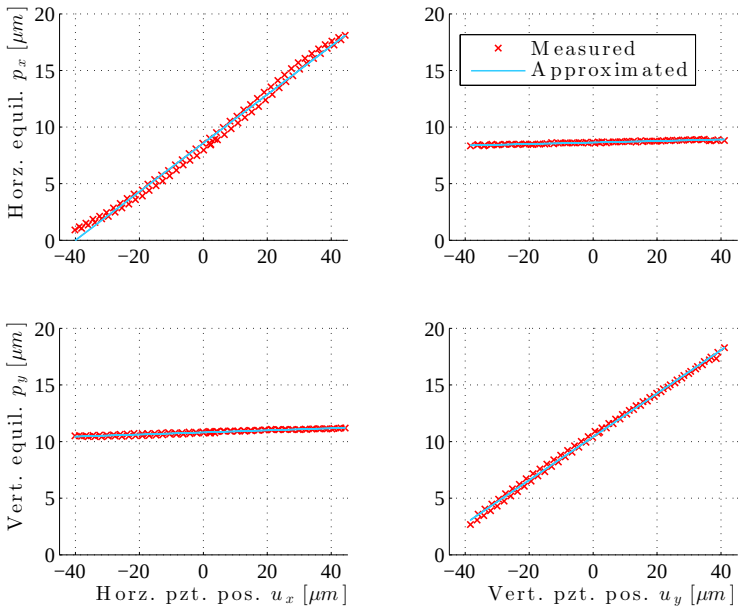

Figure 5: Steady state characterization of input-output gains at $\bar{P}_{\text{inj}} = 6bar$, $\bar{\Omega} = 0rpm$: the experimental data reveal a linear mapping from $\mathbf{u}$ to lateral disc position $\mathbf{p}$.

3.2. Grey-Box Model of Rotor-Bearing System

A combined model of the rotor and the gas bearing can be set up as a 2 DOF coupled mass-spring-damper equivalent in a neighbourhood around the two first eigenfrequencies. For given constant shaft rotational speed $\Omega = \bar{\Omega}$ and injection pressure $P_{\text{inj}} = \bar{P}$, the model reads:

$$\mathcal{M}\ddot{\mathbf{p}}(t) + (\mathcal{D} + \bar{\Omega}\mathcal{G})\dot{\mathbf{p}}(t) + \mathcal{K}\mathbf{p}(t) = \mathbf{f}(t), \tag{4}$$

where $\mathcal{M} = \text{diag}(m, m)$ is the mass matrix, $\mathcal{D}$ is the damping matrix, $\mathcal{G}$ represents the antisymmetric gyroscopic effect, and $\mathcal{K}$ is the stiffness matrix, all of dimension 2×2. The matrices $\mathcal{D}, \mathcal{G}$, and $\mathcal{K}$ are known to vary with injection pressure and rotational speed. The right hand side of Eq. 4 includes external forces $\mathbf{f}(t)$ acting on the shaft, which includes mass unbalance, external disturbances and active forces controlled with help of the piezoactuators. Section 3.5 shows how to subtract the response from the unknown mass unbalance. Thus, by ensuring no impacts occur during collected data sets, only the response from active forces remain. These are not easily modelled due to the compressibility of air, which causes memory effect as known from Cummins equation [27]. The memory effect can effectively be modelled as time delays $\boldsymbol{\tau} = [\tau_x, \tau_y]^{\text{T}}$ from piezoactuator position to force applied on the shaft. Section 3.1 showed that the disc lateral movement could be approximated proportional to $\mathbf{u}$, and it is therefore reasonable to assume that the active forces are also proportional to the delayed signal $\mathbf{u}_\tau(t) \triangleq [u_x(t-\tau_x), u_y(t-\tau_y)]^{\text{T}}$ with a gain $\mathcal{B}_p$:

$$\mathcal{M}\ddot{\mathbf{p}}(t) + (\mathcal{D} + \bar{\Omega}\mathcal{G})\dot{\mathbf{p}}(t) + \mathcal{K}\mathbf{p}(t) = \mathcal{B}_p\mathbf{u}_\tau(t), \quad \mathbf{u}_\tau(t) \triangleq [u_x(t-\tau_x), u_y(t-\tau_y)]^{\text{T}} \tag{5}$$

This suggests a model structure for identification. With a model structure known, the identification of the rotor-bearing system parameters is sought through grey-box identification. The grey-box modelling is eased by reformulation of the dynamics Eq. 5 to state space form, where a suitable choice of states is the lateral movement and velocity of the disc $\mathbf{x} \triangleq [p_x, p_y, \dot{p}_x, \dot{p}_y]^{\text{T}}$. The output is $\mathbf{y}_b = \mathcal{C}\mathbf{x} = \mathbf{p}$. The very simple model structure inevitably gives rise to modelling errors, which are included as process noise $\mathbf{v}(t)$. Measurement noise is modelled as an additive signal $\mathbf{w}(t)$. This combination of process noise and measurement noise can be reduced to one equivalent noise term $\mathbf{d}_b(t)$ entering both the state and the output equation [26]. Therefore model errors and measurement noise are included as a

stochastic additive signal $\mathbf{d}_b(t)$ entering both through an input gain $\boldsymbol{\mathcal{B}}_d$ and the measurements directly:

$$\begin{aligned}\dot{\mathbf{x}}(t) &= \boldsymbol{\mathcal{A}}\mathbf{x}(t) + \boldsymbol{\mathcal{B}}\mathbf{u}_\tau(t) + \boldsymbol{\mathcal{B}}_d\mathbf{d}_b(t), \quad \mathbf{x}(0) = \mathbf{x}_0,\\ \mathbf{y}(t) &= \boldsymbol{\mathcal{C}}\mathbf{x}(t) + \mathbf{d}_b(t),\end{aligned} \tag{6}$$

where the system-, input gain-, and output matrix are:

$$\boldsymbol{\mathcal{A}} = \begin{bmatrix}\mathbf{0} & \mathbf{I}\\ \mathbf{K} & \mathbf{D}\end{bmatrix}, \quad \boldsymbol{\mathcal{B}} = \begin{bmatrix}\mathbf{0}\\ \mathbf{B}\end{bmatrix}, \quad \boldsymbol{\mathcal{B}}_d = \begin{bmatrix}\mathbf{0}\\ \mathbf{B}_d\end{bmatrix}, \quad \boldsymbol{\mathcal{C}} = \begin{bmatrix}\mathbf{I} & \mathbf{0}\end{bmatrix}, \tag{7}$$

and $\mathbf{D} \triangleq -\boldsymbol{\mathcal{M}}^{-1}(\boldsymbol{\mathcal{D}} + \bar{\Omega}\boldsymbol{\mathcal{G}})$, $\mathbf{K} \triangleq -\boldsymbol{\mathcal{M}}^{-1}\boldsymbol{\mathcal{K}}$, and $\mathbf{B} \triangleq \boldsymbol{\mathcal{M}}^{-1}\boldsymbol{\mathcal{B}}_p$ are matrices to be identified along with the disturbance gain $\mathbf{B}_d$. $\mathbf{0}$ and $\mathbf{I}$ are zero-, and identity matrices respectively. $\mathbf{K}$, $\mathbf{D}$ and $\mathbf{B}$ are thus equivalent to stiffness, damping and input gain scaled by the mass matrix. In other words, $\boldsymbol{\mathcal{M}}$ is assumed to be the identity matrix. The equivalent stiffness therefore has units $[N/(kgm)]$, the equivalent damping has units $[Ns/(kgm)]$ and the equivalent input gain has units $[N/(kgm)]$, and they are simply referred to as stiffness, damping and input gain. Using only the measured piezoactuator position as input, the model in the Laplace domain reads:

$$\begin{bmatrix}p_x(s)\\ p_y(s)\end{bmatrix} = \underbrace{\overbrace{\begin{bmatrix}G_{b,xx}(s) & G_{b,xy}(s)\\ G_{b,yx}(s) & G_{b,yy}(s)\end{bmatrix}}^{\triangleq \mathbf{G}_b(s)} \overbrace{\begin{bmatrix}e^{-\tau_x s} & 0\\ 0 & e^{-\tau_y s}\end{bmatrix}}^{\triangleq \mathbf{G}_\tau(s)}}_{\triangleq \mathbf{G}_{rb}(s)} \begin{bmatrix}u_x(s)\\ u_y(s)\end{bmatrix}, \tag{8}$$

in which $\{G_{b,xx}, G_{b,xy}, G_{b,yx}, G_{b,yy}\}$ are the individual transfer functions, and τ_x and τ_y are the delays from the pressure build-up in the gas film active forces. The time delay $\boldsymbol{\tau}$ is small, but not negligible. It is not easy to estimate directly; hence a first order Padé approximation is used instead, which gives:

$$\mathbf{G}_\tau(s) \approx \mathbf{G}_{\tilde{\tau}}(s) \triangleq \begin{bmatrix}G_{\tilde{\tau},x}(s) & 0\\ 0 & G_{\tilde{\tau},y}(s)\end{bmatrix}, \quad G_{\tilde{\tau},j}(s) \triangleq \frac{1 - \frac{\tau_j}{2}s}{1 + \frac{\tau_j}{2}s}, \tag{9}$$

Equation 9 has an equivalent state space description with state vector denoted $\mathbf{x}_\tau$, and matrices $\boldsymbol{\mathcal{A}}_\tau, \boldsymbol{\mathcal{B}}_\tau, \boldsymbol{\mathcal{C}}_\tau, \boldsymbol{\mathcal{D}}_\tau$. The controllable rotor-bearing model emerges from substitution of the Padé approximated time delay Eq. 9 into Eq. 6:

$$\begin{aligned}\overbrace{\begin{bmatrix}\dot{\mathbf{x}}(t)\\ \dot{\mathbf{x}}_\tau(t)\end{bmatrix}}^{\triangleq \dot{\mathbf{x}}_b(t)} &= \overbrace{\begin{bmatrix}\boldsymbol{\mathcal{A}} & \boldsymbol{\mathcal{B}}\boldsymbol{\mathcal{C}}_\tau\\ \mathbf{0} & \boldsymbol{\mathcal{A}}_\tau\end{bmatrix}}^{\triangleq \boldsymbol{\mathcal{A}}_b} \overbrace{\begin{bmatrix}\mathbf{x}(t)\\ \mathbf{x}_\tau(t)\end{bmatrix}}^{\triangleq \mathbf{x}_b(t)} + \overbrace{\begin{bmatrix}\boldsymbol{\mathcal{B}}\boldsymbol{\mathcal{D}}_\tau\\ \boldsymbol{\mathcal{B}}_\tau\end{bmatrix}}^{\triangleq \boldsymbol{\mathcal{B}}_b} \mathbf{u}(t) + \overbrace{\begin{bmatrix}\boldsymbol{\mathcal{B}}_d\\ \mathbf{0}\end{bmatrix}}^{\triangleq \boldsymbol{\mathcal{B}}_{d,b}} \mathbf{d}_b(t), \quad \mathbf{x}_b(0) = \mathbf{x}_{b0}\\ \mathbf{y}_b &= \overbrace{\begin{bmatrix}\boldsymbol{\mathcal{C}} & \mathbf{0}\end{bmatrix}}^{\triangleq \boldsymbol{\mathcal{C}}_b(t)} \mathbf{x}_b(t) + \mathbf{d}_b(t),\end{aligned} \tag{10}$$

where $\mathbf{x}_b$ is the concatenated state vector, $\boldsymbol{\mathcal{A}}_b, \boldsymbol{\mathcal{B}}_b, \boldsymbol{\mathcal{B}}_{d,b}$ and $\boldsymbol{\mathcal{C}}_b$ are the state space matrices. Figure 6 shows an overview of the rotor-bearing model. The signal $\mathbf{d}_b$ models the differences between measured and model response.

The parameters of Eqs. 7 and 9 in Eq. 10 are identified by recasting the problem to a model parametrised in $\boldsymbol{\theta}_b \triangleq \{\mathbf{K}, \mathbf{D}, \mathbf{B}, \boldsymbol{\tau}, \mathbf{B}_d, \mathbf{x}_{b0}\}$ as $\mathfrak{M}_b(\boldsymbol{\theta}_b)$. Each matrix $\mathbf{K}, \mathbf{D}, \mathbf{B}, \mathbf{B}_d$ has four elements denoted by small letters and subscripts xx, xy, yx, yy, e.g. $\mathbf{K} = \left[\begin{smallmatrix}k_{xx} & k_{xy}\\ k_{yx} & k_{yy}\end{smallmatrix}\right]$. The initial state $\mathbf{x}_{b0}$ has six elements denoted by $\hat{x}_{j,0}$, $j \in \{1, 2, 3, 4, 5, 6\}$. The corresponding estimates are $\hat{\boldsymbol{\theta}}_b \triangleq \{\hat{\mathbf{K}}, \hat{\mathbf{D}}, \hat{\mathbf{B}}, \hat{\boldsymbol{\tau}}, \hat{\mathbf{B}}_d, \hat{\mathbf{x}}_{b0}\} = \left[\hat{k}_{xx}, \hat{k}_{xy}, \hat{k}_{yx}, \hat{k}_{yy}, \hat{d}_{xx}, \ldots, \hat{x}_{6,0}\right]^{\mathrm{T}}$. The model then reads:

$$\mathfrak{M}_b(\boldsymbol{\theta}_b) : \begin{cases}\dot{\mathbf{x}}_b(t) = \boldsymbol{\mathcal{A}}_b(\boldsymbol{\theta}_b)\mathbf{x}_b(t) + \boldsymbol{\mathcal{B}}_b(\boldsymbol{\theta}_b)\mathbf{u}(t) + \boldsymbol{\mathcal{B}}_{d,b}(\boldsymbol{\theta}_b)\mathbf{d}_b(t), \quad \mathbf{x}_b(0) = \mathbf{x}_{b0}(\boldsymbol{\theta}_b)\\ \mathbf{y}_b(t) = \boldsymbol{\mathcal{C}}_b\mathbf{x}_b(t) + \mathbf{d}_b(t)\end{cases} \tag{11}$$

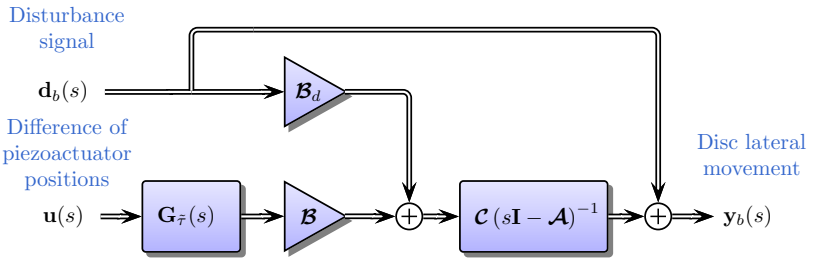

Figure 6: Overview of the rotor-bearing model: the difference of piezoactuator positions $\mathbf{u}$ enters as input into the Padé approximated delays modelling the fluid memory effect. The signal $\mathbf{d}_b$ models the differences between measured and model response including measurement noise.

3.3. Grey-Box Model of Piezoactuators

A similar model can be set up for the PD-controlled piezoactuator pairs. Each pair of piezoactuators can be modelled as a second order low-pass filter. The piezoactuator dynamics is written as transfer functions with gains $\kappa_{a,j}$ and two poles $p_{1,j}$, and $p_{2,j}$, where the subscript j refers to the pair of horizontal (x) or vertical (y) piezoactuators. Considering the commanded reference position as input, the piezoactuator dynamics $\mathbf{G}_{act}$ then reads:

$$\begin{bmatrix} u_x(s) \\ u_y(s) \end{bmatrix} = \underbrace{\begin{bmatrix} G_{a,x}(s) & 0 \\ 0 & G_{a,y}(s) \end{bmatrix}}_{\triangleq \mathbf{G}_{act}} \begin{bmatrix} r_x(s) \\ r_y(s) \end{bmatrix}, \qquad G_{a,j}(s) = \frac{\kappa_{a,j}}{\left(\frac{1}{p_{1,j}}s+1\right)\left(\frac{1}{p_{2,j}}s+1\right)} \tag{12}$$

in which $G_{a,j}(s)$ is the second order filter of the specified form. The piezoactuator dynamics can also be written in state space form as a grey-box structure similar to Eq. 6 with state vector $\mathbf{x}_a$. Let define an equivalent modelling error term $\mathbf{d}_a$ entering as input along with the commanded piezoactuator positions $\mathbf{r}$. The output is $\mathbf{u}$, and the unknown parameters are:

$$\boldsymbol{\theta}_a \triangleq [p_{1,x},\ p_{1,y},\ p_{2,x},\ p_{2,y},\ \kappa_{a,x},\ \kappa_{a,y},\ x_{a1,0},\ x_{a2,0},\ x_{a3,0},\ x_{a4,0}]^{\mathrm{T}}, \tag{13}$$

thus the actuator model $\mathfrak{M}_a(\boldsymbol{\theta}_a)$ has been set up, which reads:

$$\mathfrak{M}_a(\boldsymbol{\theta}_a): \begin{cases} \dot{\mathbf{x}}_a(t) = \boldsymbol{\mathcal{A}}(\boldsymbol{\theta}_a)\mathbf{x}_a(t) + \boldsymbol{\mathcal{B}}(\boldsymbol{\theta}_a)\mathbf{r}(t) + \boldsymbol{\mathcal{B}}_{d,a}(\boldsymbol{\theta}_a)\mathbf{d}_a(t), \quad \mathbf{x}_a(0) = \mathbf{x}_{a0}(\boldsymbol{\theta}_a) \\ \mathbf{u}(t) = \boldsymbol{\mathcal{C}}_a\mathbf{x}_a(t) + \mathbf{d}_a(t) \end{cases} \tag{14}$$

3.4. Description of Experiments

The sought model should represent the controllable gas bearing over the entire operating range. Previous work [22] show that the gas bearing coefficients mainly depend on two parameters: the rotational speed Ω and injection pressure P_{inj}, which can vary within $\Omega \in [0;6]krpm$ and $P_{\mathrm{inj}} \in [3;7]bar$. Locally valid models can therefore be identified from data sets collected over a grid of these two parameters. Grid points are chosen in the sets $\bar{P}_{\mathrm{inj}} \in \{3,4,5,6,7\}bar$ and rotational speeds $\bar{\Omega} \in \{0,4,6\}krpm$. Five to six data sets are collected at each grid point $(\bar{P}_{\mathrm{inj}}, \bar{\Omega})$, and a model is identified from each data set. During the collected data sets, identifiability of the parameters is ensured by commanding a pseudo-random binary sequence (PRBS) to the piezoactuators $\mathbf{r}(t)$, where the inputs are stepped randomly and mutually independently from $-1V$ to $1V$ at fixed sampling instants. The eigenfrequencies are very under-damped, and care should be taken to avoid rub due to over-excitation. The piezoactuator position references $\mathbf{r}(t)$ and measured difference of piezoactuator positions $\mathbf{u}(t)$ are logged as input and output respectively for the actuator submodel and $\mathbf{u}(t)$ and the lateral disc movement $\mathbf{p}(t)$ are logged as input and outputs for the rotor-bearing model.

3.5. Prefiltering

Prefiltering is required before carrying out the identification to remove offsets, response from run-out, and mass unbalance from the raw position measurements $\mathbf{p}_{raw}$. A data set is collected at each investigated operational condition $(\bar{P}_{\mathrm{inj}}, \bar{\Omega})$. Each data set allows generation of a filter $\mathcal{F}_r$ to remove run-out and unbalance response from the

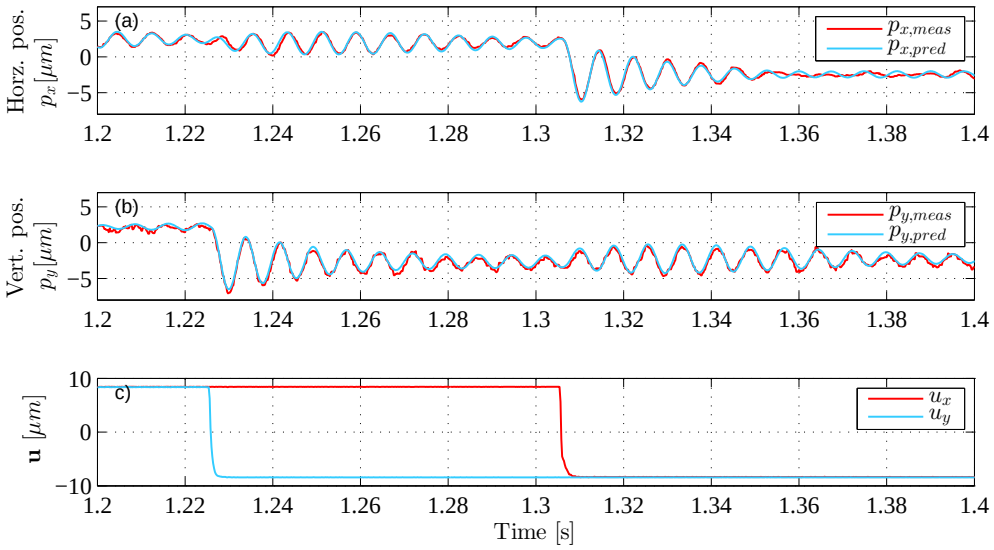

Figure 7: Example of identification from data set collected at $\bar{P}_{\text{inj}} = 5bar, \bar{\Omega} = 6.0krpm$, here a zoom in time interval in the interval $t \in [1.2 : 1.4]s$. The piezoactuator positions $[u_x, u_y]$ shown in c) cause disc vibrations. The lateral disc movement $\mathbf{p}_{meas} = [p_x, p_y]$ and the simulated movement using the identified model $\mathbf{p}_{pred} = [\hat{p}_x, \hat{p}_y]$ subject to same excitation is shown in a) and b). The model predicts both the direct and the cross coupling oscillations.

lateral disc movement measurements. During these experiments, the piezoactuators are kept stationary, which allows mapping of the measured response $\mathbf{p}_{raw}$ as function of the angular position of the rotor ϕ. Thereby the filtered lateral disc movement is $\mathbf{p}(t) = \mathbf{p}_{raw}(t) - \mathcal{F}_r(\phi(t))$. For the signals collected for identification, the mean lateral disc position is subtracted from each data set, and a median filter of size 3 is used to reduce measurement noise from the disc movement measurements. The compensation for run-out and unbalance significantly improves the signal quality and allows micrometer precision measurement of the response from perturbing the piezoactuators.

3.6. Identification of Rotor-Bearing Models

The optimal rotor-bearing model $\mathfrak{M}_b(\boldsymbol{\theta}_b^\star)$ from each data set is chosen as the one associated with the minimum cost of a prediction error cost function $W_b(\boldsymbol{\theta}_b) \triangleq \sum_{t=1}^{N} \boldsymbol{\epsilon}(t)^{\mathrm{T}} \boldsymbol{\epsilon}(t)$, where the prediction error $\boldsymbol{\epsilon}$ is defined as the difference between the one step ahead measured and the predicted output $\boldsymbol{\epsilon}(t) \triangleq \mathbf{p}(t) - \hat{\mathbf{p}}(t)$. The minimum is sought using the prediction error method (PEM) [26], such that the optimal parameter set reads:

$$\boldsymbol{\theta}_b^\star = \min_{\boldsymbol{\theta}_b} W_b(\boldsymbol{\theta}_b) \tag{15}$$

The model update iterations should stop when the parameter estimates converge. This convergence is decided when the relative improvement norm is less than the bound 10^{-4}. A rotor-bearing model $\mathfrak{M}_b(\hat{\boldsymbol{\theta}}_b)$ is identified from each data set $\{\mathbf{u}(t), \mathbf{p}(t)\}$. The identified model is simulated using the measured input sequence to generate the model predicted response to allow comparison. Figure 7 shows an example of measured lateral disc movement $\mathbf{p}_{meas} = [p_{x,meas}, p_{y,meas}]^{\mathrm{T}}$ and their predicted $\mathbf{p}_{pred} = [p_{x,pred}, p_{y,pred}]^{\mathrm{T}}$ for a part of one of the 86 data sets. A step signal commanded to the piezoactuators in one direction generates disc vibrations in both orthogonal directions due to the cross-coupling effect from the gas film forces and the gyroscopic moment. The identified model predicts direct and cross-coupling oscillations well. All the available data sets give similar results.

The fourteen key parameters being stiffness, damping, input gain and time delay estimates are comparable across identified models, and they determine the eigenfrequencies, the static gains and delays of the models. Parameters such as the initial state $\hat{\mathbf{x}}_{b0}$, and disturbance gain $\hat{\mathbf{B}}_{d,b}$ are more descriptive for the particular dataset and are not relevant to compare across identified models. The key parameters are treated further in Sec. 4.

Parameter	$p_{1,x}$ $[rad/s]$	$p_{2,x}$ $[rad/s]$	$p_{1,y}$ $[rad/s]$	$p_{2,y}$ $[rad/s]$	$\kappa_{a,x}$ $[m/m]$	$\kappa_{a,y}$ $[m/m]$
Value	3078	8143	2452	6494	1.863	1.865

Table 2: Actuator model parameters.

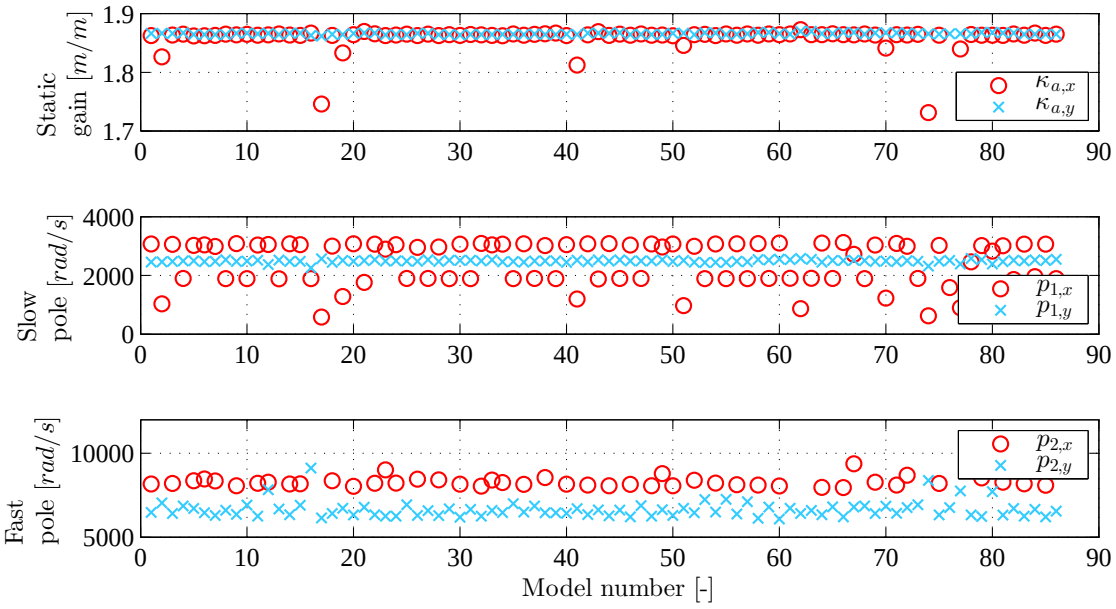

Figure 8: Estimated gains $\kappa_{a,x}, \kappa_{a,y}$, slow poles $p_{1,x}, p_{1,y}$, and fast poles $p_{2,x}, p_{2,y}$ of the actuator models from Eq. 12 across the models identified from different data sets.

3.7. Identification of Actuator Models

The actuator dynamics is identified using the same procedure as in Sec. 3.6. An actuator model $\mathfrak{M}_a(\hat{\boldsymbol{\theta}}_a)$ is identified from each data set $\{\mathbf{r}(t), \mathbf{u}(t)\}$. Figure 8 shows the estimated gains and poles $\{\kappa_x, \kappa_y, p_{1,x}, p_{2,x}, p_{1,y}, p_{2,y}\}$ of the identified models using Eq. 12 across the data sets. The actuator parameters do not vary over the range of injection pressure and rotational speed, but there are outliers in the pole and gain estimates. There are two main reasons for this. The well damped actuator dynamics does not show clear resonances. Further, the step frequency of the excitation signals is low compared to the dynamics of the piezoactuators. Higher frequent stepping intervals in the PRBS signals would however excite the under-damped eigenfrequencies of the bearing dynamics and cause big amplitude shaft oscillations.

Since the actuator dynamics are found to be independent of rotational speed and injection pressure, a nominal model is chosen as the one with the highest mean of fit-percentages in cross-validation. This is No. 39, which has parameters listed in Table 2.

3.8. Model Cross-Validation

The quality of the identified models is assessed by cross-validating them on other data sets collected at similar operational conditions.

A simulation compares how well each identified model is at predicting the response for a cross-validation data set. Model j identified from dataset j is validated on dataset $j+1$ collected at the same rotational speed and injection pressure. Figure 9 shows a histogram of the cross-validation fits. The horizontal fit mean value is $\mu_{bh} = 81.1\%$ and its standard deviation is $\sigma_{bh} = 2.66\%$, and the vertical fit mean value is $\mu_{bv} = 85.1\%$ and its standard deviation is $\sigma_{bv} = 3.37\%$. These are high fit percentages indicating the models can well describe the behaviour of the rotor-bearing system. The simulation residual $\boldsymbol{\epsilon}(t)$ defined as the difference between measured response $\mathbf{p}$ and predicted response $\hat{\mathbf{p}}(\hat{\boldsymbol{\theta}}_b)$ should ideally be white noise. This is not the case, and the residual will to some extent be cross-correlated with the inputs. This is a penalty of the simple model structure. The infinity norm of the residuals is, however, small for all 86 datasets, indicating good significance of the results.

Similar analysis is made for the piezoactuator submodel. The piezoactuator model is cross-validated against the other piezoactuator datasets. The results are shown in Fig. 10. The actuator horizontal fit mean value is $\mu_{ah} = 98.34\%$ and its standard deviation is $\sigma_{ah} = 0.074\%$, whereas the fit percentages for the pair of vertical piezoactuators have $\mu_{av} = 99.42\%$ and its standard deviation is $\sigma_{av} = 0.058\%$. The lower horizontal fits match well with the bigger variation in parameters of the horizontal piezoactuators from Fig. 8.

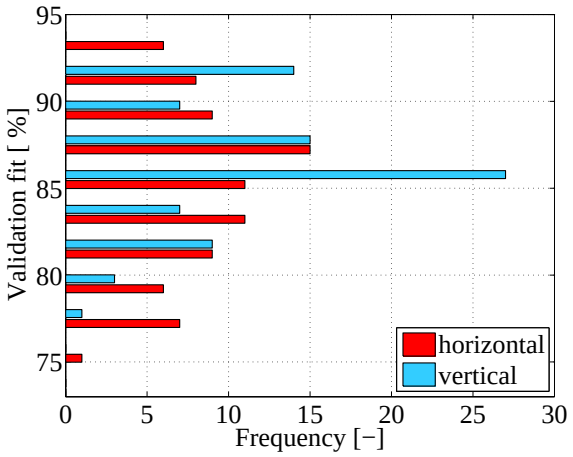

Figure 9: Cross-validation fit percentages of the horizontal and vertical residuals in validation of the identified bearing submodels cross-validated on other data sets.

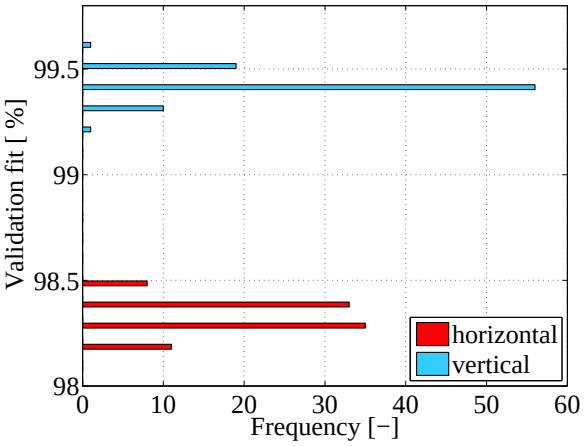

Figure 10: Horizontal and vertical validation fit percentages of the identified actuator submodels cross-validated on other data sets.

4. Linear Parameter Varying Model of Rotor-Bearing System

The locally identified models provide the basis for construction of a parametrised rotor-bearing model valid over the operating range. The model is developed in three steps: the first step is the approximation of each key parameter from the 86 parameter estimates onto smooth surfaces. These individually approximated terms are used in the second step to assemble a linear parameter varying model of the rotor-bearing system parametrised in speed and injection pressure. The last step is to cascade the linear parameter varying model with the piezoactuator model to obtain the model of the entire rotor-bearing-actuator system. The steps are elaborated in the following.

The rotor-bearing model parameters are expected to depend continuously on injection pressure and rotational speed. Each key parameter is therefore approximated onto a polynomial surface. A second order polynomial is chosen to avoid over-fitting. Thereby the identified stiffness, damping and gain matrix coefficients $(\cdot)_{ij}$, where $(\cdot) \in \{k, c, b\}$ and $i, j \in \{x, y\}$ (e.g. k_{xy}) and the time delays τ_x and τ_y are modelled as:

$$\begin{aligned}
k_{ij}(\Omega, P_{\text{inj}}) =& k_{0,ij} + k_{1,ij}P_{\text{inj}} + k_{2,ij}\Omega + k_{3,ij}\Omega P_{\text{inj}} + k_{4,ij}P_{\text{inj}}^2 + k_{5,ij}\Omega^2 \\
c_{ij}(\Omega, P_{\text{inj}}) =& c_{0,ij} + c_{1,ij}P_{\text{inj}} + c_{2,ij}\Omega + c_{3,ij}\Omega P_{\text{inj}} + c_{4,ij}P_{\text{inj}}^2 + c_{5,ij}\Omega^2 \\
b_{ij}(\Omega, P_{\text{inj}}) =& b_{0,ij} + b_{1,ij}P_{\text{inj}} + b_{2,ij}\Omega + b_{3,ij}\Omega P_{\text{inj}} + b_{4,ij}P_{\text{inj}}^2 + b_{5,ij}\Omega^2 \\
\tau_i(\Omega, P_{\text{inj}}) =& \tau_{0,i} + \tau_{1,i}P_{\text{inj}} + \tau_{2,i}\Omega + \tau_{3,i}\Omega P_{\text{inj}} + \tau_{4,i}P_{\text{inj}}^2 + \tau_{5,i}\Omega^2
\end{aligned} \tag{16}$$

This describes a surface in space, whose cross-sections are a parabola. The parameters of the polynomial models are fitted using linear least squares and the calculated regression coefficients are listed in table B.6. Note the units of the stiffness, damping and input gain equivalents as described in Sec. 3. The stiffness coefficients $\{\hat{k}_{xx}, \hat{k}_{xy}, \hat{k}_{yx}, \hat{k}_{yy}\}$ are shown in Fig. 11 along with their polynomial approximations. Similarly Figs. 12 and 13 show the estimated damping coefficients and input gains with the corresponding polynomial approximations. The variation of each key parameter's estimate for a fixed operational condition is small, indicating a good consistency across different data sets.

Figures 14 and 15 show comparisons of the estimated time delays between the identified models and their polynomial approximations. It is interesting to note that the delay is bigger in the horizontal direction. The RMS deviation

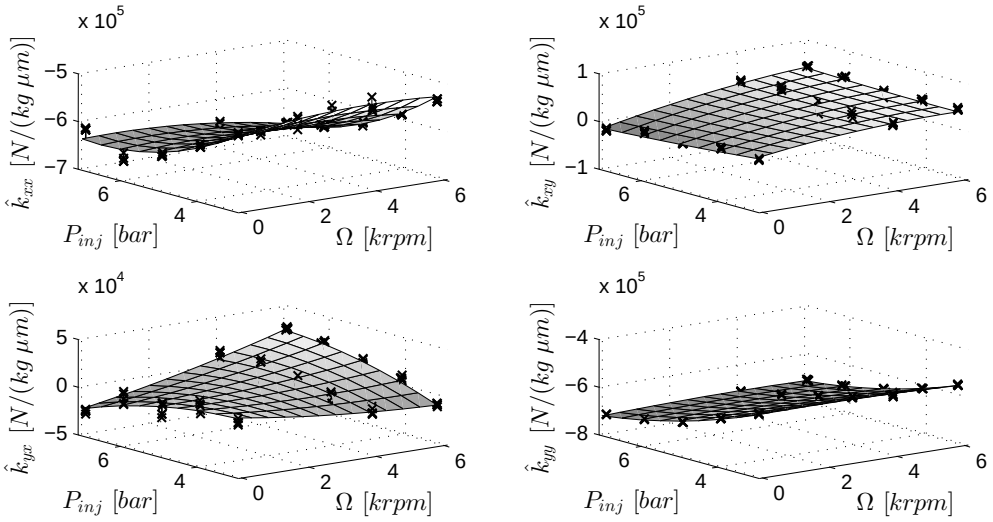

Figure 11: Identified stiffness coefficients as function of injection pressure P_{inj} ($1bar = 0.1MPa$) and rotational speed Ω, along with 2^{nd} order polynomial fit, assisting lines indicate 3D location of the parameter estimates.

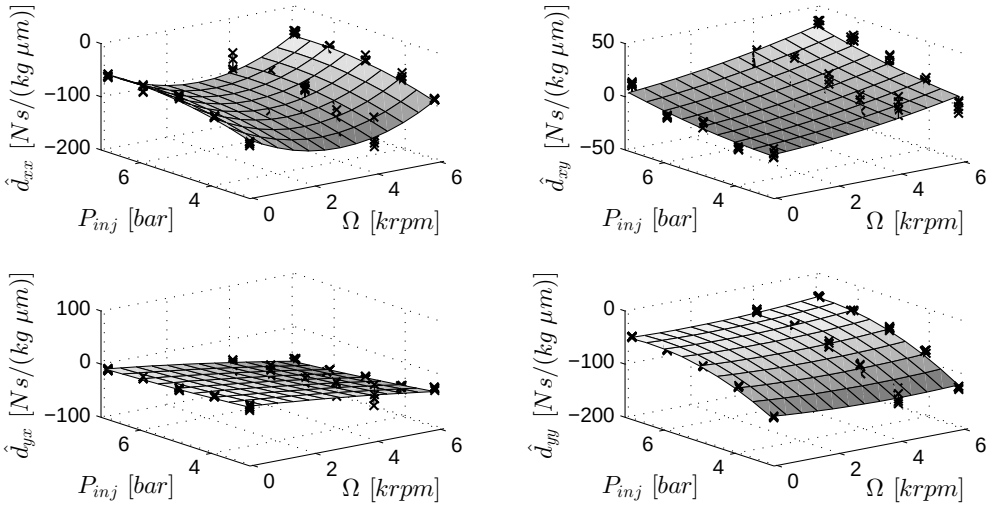

Figure 12: Identified damping coefficients as function of injection pressure P_{inj} ($1bar = 0.1MPa$) and rotational speed Ω, along with 2^{nd} order polynomial fit, assisting lines indicate 3D location of the parameter estimates.

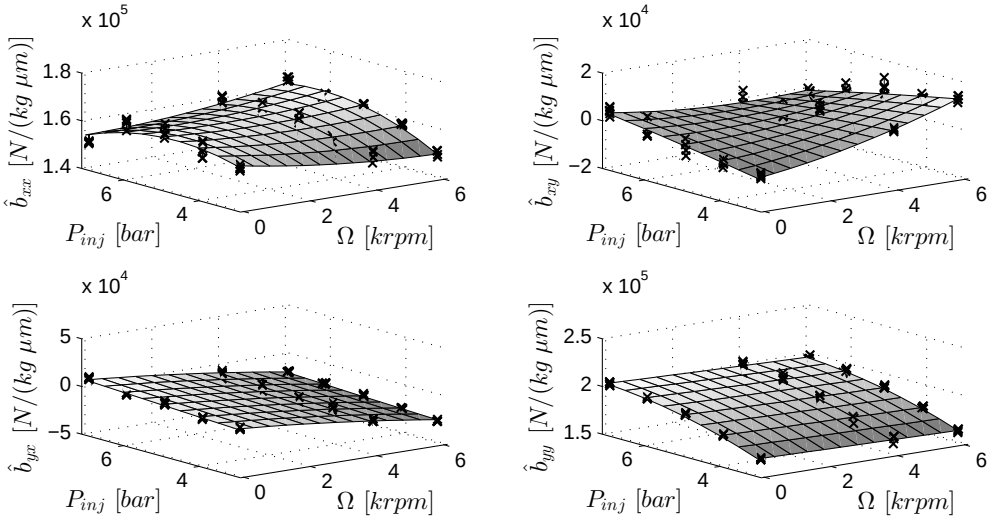

Figure 13: Identified input gain coefficients as function of injection pressure P_{inj} ($1bar = 0.1MPa$) and rotational speed Ω, along with 2^{nd} order polynomial fit, assisting lines indicate 3D location of the parameter estimates.

for horizontal and vertical time delays are $\Delta\tau_{x,RMS} = 0.088ms$, $\Delta\tau_{y,RMS} = 0.041ms$. Compared to the sampling period of $T_s = 0.2ms$, the variation in estimated time delays is small, and since their identification is not easy due to the combination of dynamics and time delays, the results are considered good. It is evident that for increasing pressure the time delay drops, which intuitively makes sense: a larger pressure allows a faster pressure build-up.

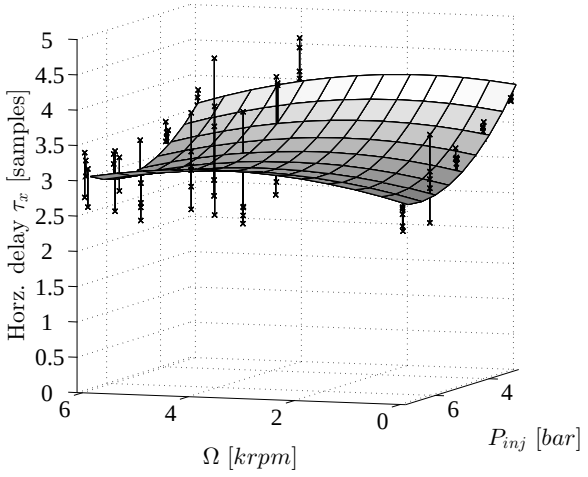

Figure 14: Identified and linear parameter varying model horizontal time delay [*samples@5kHz*] between Eq. 17 over varying speed and injection pressure, ($1bar = 0.1MPa$).

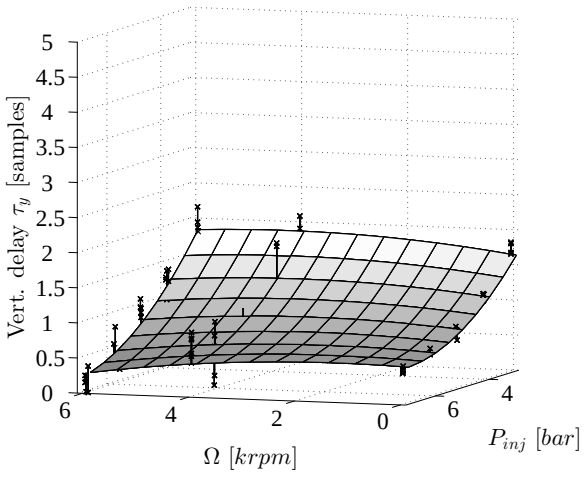

Figure 15: Identified and linear parameter varying model vertical time delay [*samples@5kHz*] between Eq. 17 over varying speed and injection pressure.

All parameters (stiffness, damping, gain terms and time delays) have been parametrised in the same manner. This in turn allows for the assembly of the linear parameter varying model:

$$\begin{aligned}\dot{\mathbf{x}}(t) =& \boldsymbol{\mathcal{A}}(\Omega, P_{\text{inj}})\mathbf{x}(t) + \boldsymbol{\mathcal{B}}(\Omega, P_{\text{inj}})\mathbf{u}_{\tilde{\tau}}(t, \Omega, P_{\text{inj}}), \quad \mathbf{u}_{\tilde{\tau}} \triangleq [u_x(t - \tau_x(\Omega, P_{\text{inj}})), u_y(t - \tau_y(\Omega, P_{\text{inj}}))]^{\mathrm{T}} \\ \mathbf{y}(t) =& \boldsymbol{\mathcal{C}}\mathbf{x}(t)\end{aligned} \tag{17}$$

Where the parameters from Eq. 16 are used to assemble the matrices:

$$\begin{aligned}
\boldsymbol{\mathcal{A}}(\Omega, P_{\text{inj}}) &= \underbrace{\begin{bmatrix} \mathbf{0} & \mathbf{I} \\ \mathbf{K}_0 & \mathbf{D}_0 \end{bmatrix}}_{\boldsymbol{\mathcal{A}}_0} + \underbrace{\begin{bmatrix} \mathbf{0} & \mathbf{0} \\ \mathbf{K}_1 & \mathbf{D}_1 \end{bmatrix}}_{\boldsymbol{\mathcal{A}}_1} P_{\text{inj}} + \underbrace{\begin{bmatrix} \mathbf{0} & \mathbf{0} \\ \mathbf{K}_2 & \mathbf{D}_2 \end{bmatrix}}_{\boldsymbol{\mathcal{A}}_2} \Omega + \underbrace{\begin{bmatrix} \mathbf{0} & \mathbf{0} \\ \mathbf{K}_3 & \mathbf{D}_3 \end{bmatrix}}_{\boldsymbol{\mathcal{A}}_3} \Omega P_{\text{inj}} + \underbrace{\begin{bmatrix} \mathbf{0} & \mathbf{0} \\ \mathbf{K}_4 & \mathbf{D}_4 \end{bmatrix}}_{\boldsymbol{\mathcal{A}}_4} P_{\text{inj}}^2 + \underbrace{\begin{bmatrix} \mathbf{0} & \mathbf{0} \\ \mathbf{K}_5 & \mathbf{D}_5 \end{bmatrix}}_{\boldsymbol{\mathcal{A}}_5} \Omega^2 \\
\boldsymbol{\mathcal{B}}(\Omega, P_{\text{inj}}) &= \begin{bmatrix} \mathbf{0} \\ \mathbf{B}(\Omega, P_{\text{inj}}) \end{bmatrix}, \quad \mathbf{B}(\Omega, P_{\text{inj}}) = \mathbf{B}_0 + \mathbf{B}_1 P_{\text{inj}} + \mathbf{B}_2 \Omega + \mathbf{B}_3 \Omega P_{\text{inj}} + \mathbf{B}_4 P_{\text{inj}}^2 + \mathbf{B}_5 \Omega^2 \\
\boldsymbol{\tau}(\Omega, P_{\text{inj}}) &= \boldsymbol{\tau}_0 + \boldsymbol{\tau}_1 P_{\text{inj}} + \boldsymbol{\tau}_2 \Omega + \boldsymbol{\tau}_3 \Omega P_{\text{inj}} + \boldsymbol{\tau}_4 P_{\text{inj}}^2 + \boldsymbol{\tau}_5 \Omega^2
\end{aligned} \tag{18}$$

This linear parameter varying model has rotational speed and injection pressure as scheduling parameters, and for constant parameters $(\Omega, P_{\text{inj}}) = (\bar{\Omega}, \bar{P}_{\text{inj}})$, the bearing transfer function can then be defined:

$$\mathbf{G}_{rb}(s, \bar{\Omega}, \bar{P}_{\text{inj}}) = \mathbf{G}_b(s, \bar{\Omega}, \bar{P}_{\text{inj}}) \mathbf{G}_{\tilde{\tau}}(s, \bar{\Omega}, \bar{P}_{\text{inj}}), \quad \mathbf{G}_b(s, \bar{\Omega}, \bar{P}_{\text{inj}}) = \boldsymbol{\mathcal{C}} \left(s\mathbf{I} - \boldsymbol{\mathcal{A}}(\bar{\Omega}, \bar{P}_{\text{inj}}) \right)^{-1} \boldsymbol{\mathcal{B}}(\bar{\Omega}, \bar{P}_{\text{inj}}) \tag{19}$$

The linear parameter varying model in Eq. 17 is valid if it preserves the main characteristics for the rotor-bearing system such as natural frequencies, damping factors and static gains $\mathbf{G}_{dc} = \mathbf{G}_{rb}(0, \bar{\Omega}, \bar{P}_{\text{inj}}) = \left[\begin{smallmatrix} g_{xx} & g_{xy} \\ g_{yx} & g_{yy} \end{smallmatrix} \right]$. These characteristics can be directly calculated from the experimentally identified models and compared to those of developed model $\mathbf{G}_{rb}(s, \bar{\Omega}, \bar{P}_{\text{inj}})$. The identified models have two pairs of complex conjugate eigenvalues, which can be listed as two natural frequencies ω_1, ω_2 and corresponding damping factors ζ_1, ζ_2. Figure 16 shows a comparison of the natural frequencies ω_1 and ω_2 between the linear parameter varying model and the identified rotor-bearing models. The quality of the linear parameter varying model is quantified by the deviation defined for a given pressure $\bar{P}_{\text{inj}}$ and rotational speed $\bar{\Omega}$ as the difference between the identified parameter and parameter predicted using Eq. 16. The RMS deviation for the first and 2nd eigenvalue pairs are $\Delta\omega_{1,RMS} = 1.13Hz$, $\Delta\omega_{2,RMS} = 0.58Hz$ respectively.

Figure 17 shows a comparison of the damping factors of the eigenvalues. The RMS deviation for the damping factors of the first and 2nd eigenvalue are $\Delta\zeta_{1,RMS} = 0.0104[-]$ and $\Delta\zeta_{2,RMS} = 0.0063[-]$. The damping factors are in general more uncertain, which makes the polynomial approximation more uncertain. It is evident that the results collected at $\bar{\Omega} = 4krpm$ are in general more uncertain than results collected at other operational conditions. The measurement quality of the lateral disc movement relies on the quality of the filter to remove run-out and unbalance, which in turn relies on a well defined stationary mass unbalance orbit. This is not the case for the results collected around $4krpm$, where small deviations occur in the orbit, indicating non-synchronous vibration. The filter is therefore not able to eliminate the mass unbalance response. The static gain matrix is shown in Fig. 18 along with the static gains of the identified models. The maximum observed deviation is $0.016\ m/m$, and the standard deviation for each gain is $[\sigma_{g,xx}, \sigma_{g,xy}, \sigma_{g,yx}, \sigma_{g,yy}]^{\mathrm{T}} = [0.0031,\ 0.0022,\ 0.0027,\ 0.0031]^{\mathrm{T}} m/m$.

The entire model results from cascading the linear parameter varying model with the piezoactuator model Eq. 12:

$$\mathbf{G}(s, \bar{\Omega}, \bar{P}_{\text{inj}}) = \mathbf{G}_{rb}(s, \bar{\Omega}, \bar{P}_{\text{inj}}) \mathbf{G}_{act}(s), \tag{20}$$

which is readily evaluated for a given operational condition.

5. Decentralised P-control of Controllable Gas Bearing

The poor damping properties of the controllable gas bearing can be improved by means of active control. A P-controller is designed using the proposed model, which strongly increases the closed loop damping factor. Figure 19 provides an overview of the closed loop system. Experimental results for selected operational conditions validate the strong damping enhancement. Comparisons show a good agreement between the simulated and measured response, and confirms suitability of the identification procedure.

The identified models show that the direct couplings from horizontal/vertical piezoactuator to horizontal/vertical disc movement have gains an order of magnitude larger than the cross coupling gains. This makes decentralised control a feasible option. The controller should improve the damping properties and reject disturbances in a frequency range around the under-damped eigenfrequencies. Our recent work [28] show, that this is possible with a proportional controller, where an interval of positive feedback gains provide damping injection. Therefore a proportional controller

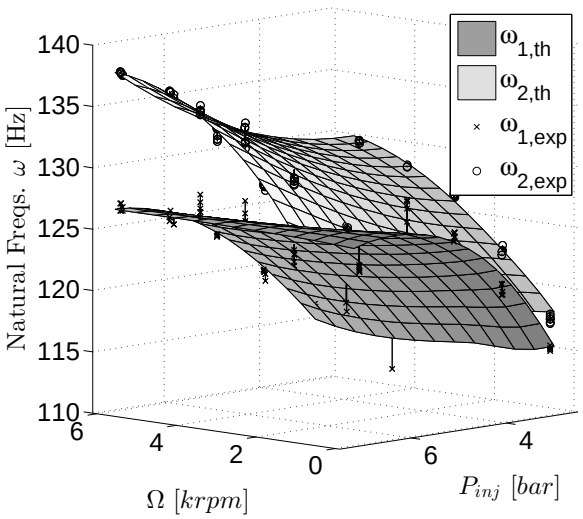

Figure 16: Natural frequencies of the experimentally identified models and the linear parameter varying model Eq. 17 over varying speed and injection pressure, ($1bar = 0.1MPa$).

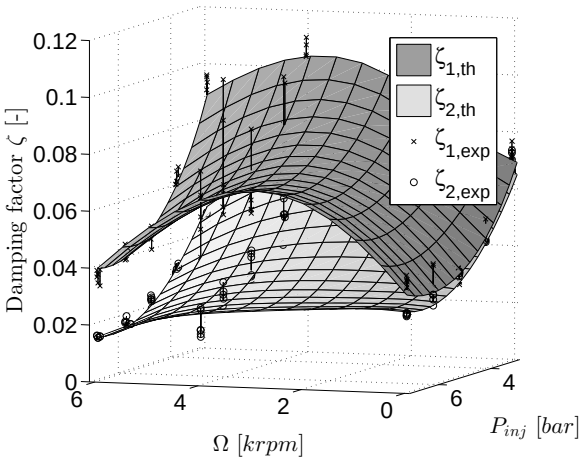

Figure 17: Damping factors of experimentally identified models and the linear parameter varying model Eq. 17 over varying speed and injection pressure, ($1bar = 0.1MPa$).

is designed for the horizontal and vertical directions to improve the damping properties. The control law is $\mathbf{r}(s) \triangleq \mathbf{K}_{pl}(s)\mathbf{p}(s)$, where the controller $\mathbf{K}_{pl}$ has the form:

$$\mathbf{K}_{pl}(s) \triangleq \begin{bmatrix} \kappa_x & 0 \\ 0 & \kappa_y \end{bmatrix} H_{lp}(s) \tag{21}$$

The controller parameters to be tuned are the proportional gains κ_x and κ_y. An n_K-th order lowpass filter $H_{lp}(s)$ is inserted to reduce controller sensitivity towards high frequency oscillations. The developed model Eq. 20 provides an excellent basis for offline design, which avoids the risk of instability during online tuning. Upon closing the loop with the controller $\mathbf{K}_{pl}$, the output sensitivity $\mathbf{S}_o$ and closed loop controller sensitivity $\mathbf{K}_{pl}\mathbf{S}_o$ can be calculated, where:

$$\mathbf{S}_o(s) \triangleq (\mathbf{I}_2 - \mathbf{G}(s)\mathbf{K}_{pl}(s))^{-1}. \tag{22}$$

The output sensitivity $\mathbf{S}_o$ and closed loop controller sensitivity $\mathbf{K}_{pl}\mathbf{S}_o$ are useful tools for tuning the controller gains. The output sensitivity both allows evaluation of the reduction in sensitivity in the desired frequency range, while at the same time evaluating the increase in sensitivity at other frequencies. Similarly the closed loop controller sensitivity $\mathbf{K}_{pl}\mathbf{S}_o$ allows inspection of the required control effort. The controller design produces positive feedback and the choices $\kappa_x = 1.1250\ m/m$,$\kappa_y = 0.99\ m/m$, increases the damping factor by a factor 9.0 and 14.5 respectively. A first order low-pass filter $H_{lp}(s) \triangleq p_{lp}/(s + p_{lp})$ with bandwidth $p_{lp} = 1000\ Hz$ is used to avoid counteraction of high frequency disturbances. The output sensitivity and closed loop controller sensitivity shown in Fig. 20 reveal the desirable properties: the sensitivity is greatly reduced close to the resonance frequencies, thus increasing horizontal and vertical damping. This comes at the cost of a disturbance amplification for low frequencies in the horizontal direction. An increase in sensitivity in some frequency interval is unavoidable due to Bode's sensitivity integral [29], and this is affordable as the mass unbalance response at these frequencies is low. Figure 21 shows the open loop magnitude response $\mathbf{p}(s) = \mathbf{G}(s)\mathbf{r}(s)$ compared to the closed loop input disturbance response $\mathbf{p}(s) = \mathbf{S}_o(s)\mathbf{G}(s)\mathbf{r}(s)$. The reduction in peak gain is evident.

5.1. Experimental Results

The increase in damping is experimentally validated by comparing the lateral disc response to impulse excitation with and without the controller proposed. Both the horizontal and vertical controllers are simultaneously active. An impact hammer is used to excite the shaft close to the controllable gas bearing while measuring the impact force to

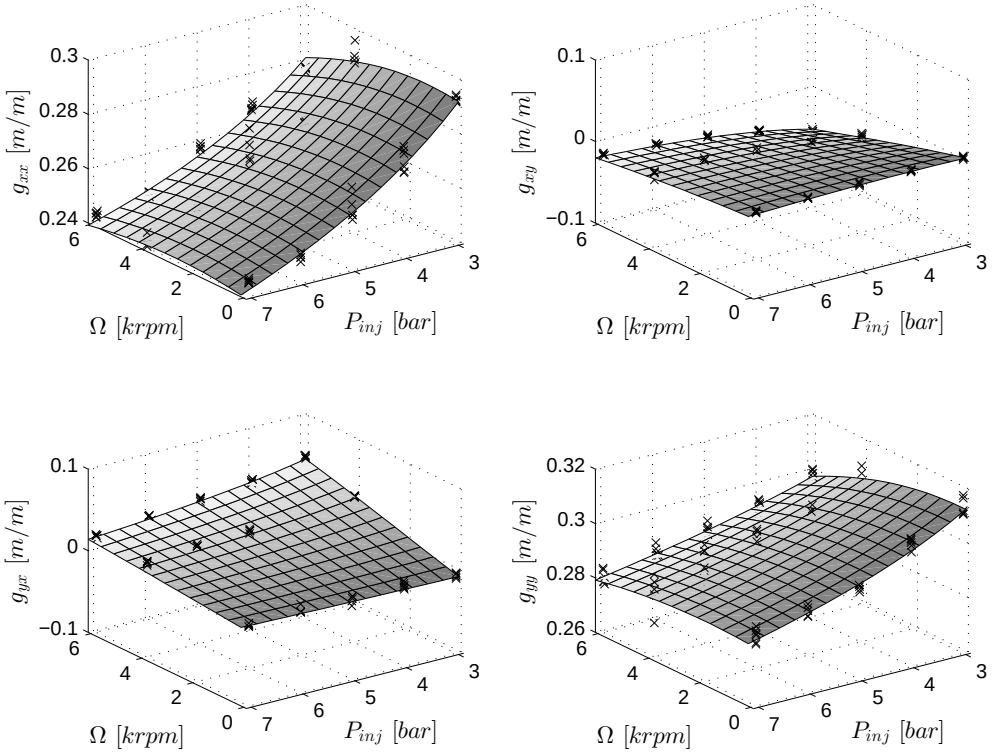

Figure 18: Comparison of static gains between experimentally identified models and the linear parameter varying model Eq. 17 over varying speed and injection pressure.

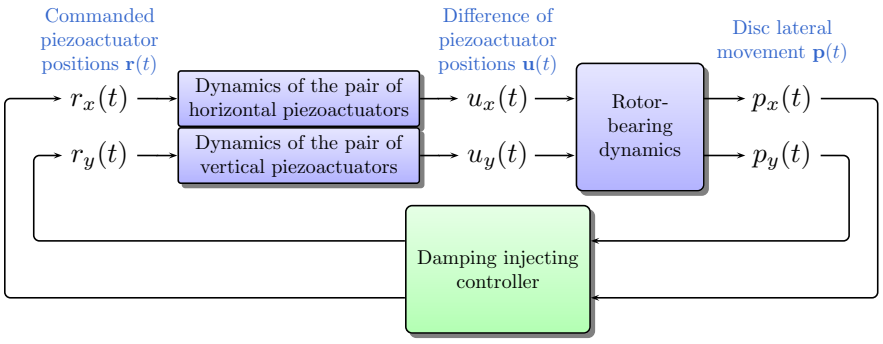

Figure 19: Block diagram of the closed loop system. The horizontal piezoactuators are decoupled from the vertical ones. The lateral disc movement is used by the feedback controller to generate piezoactuator reference positions.

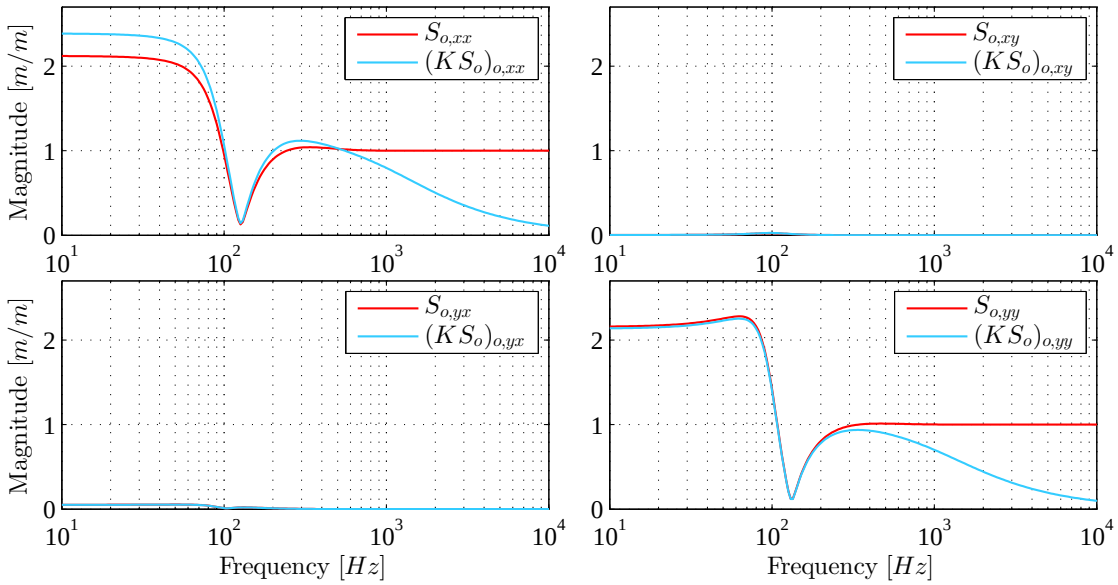

Figure 20: Output sensitivity $\mathbf{S}_o$ and closed loop controller sensitivity $\mathbf{K}_{pl}\mathbf{S}_o$ for the controller $\mathbf{K}_{pl}$.

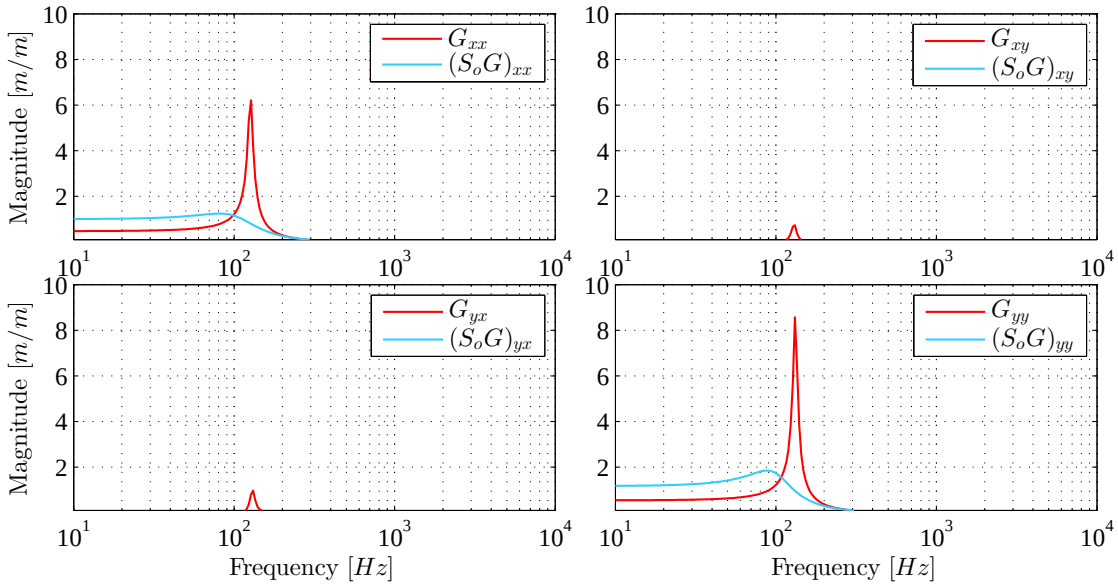

Figure 21: Bode magnitude diagram for the open loop system $\mathbf{G}$ and closed input disturbance response $\mathbf{S}_o\mathbf{G}$ for the controller $\mathbf{K}_{pl}$.

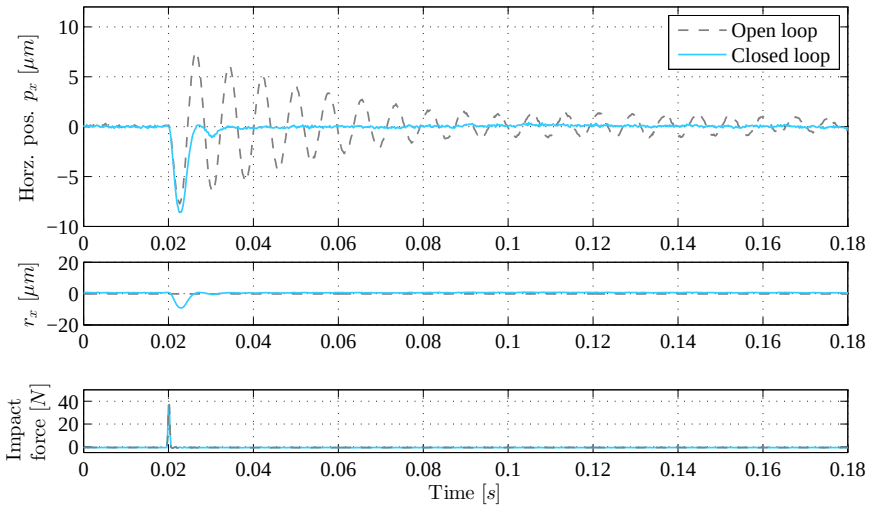

Figure 22: Horizontal open and closed loop impact responses and measured impact forces.

Natural frequency	$\omega_{1,ol}$ $[Hz]$	$\omega_{1,cl}$ $[Hz]$	$\omega_{2,ol}$ $[Hz]$	$\omega_{2,cl}$ $[Hz]$
Expected from model	126.6	99.9	132.1	105.1
Obtained Experimentally	126.3	89.9	134.4	111.6

Table 3: Expected and obtained open loop natural frequencies $\omega_{1,ol}$, $\omega_{2,ol}$ and expected and obtained closed loop natural frequencies $\omega_{1,cl}$, $\omega_{2,cl}$.

ensure equal excitation across the experiments to be compared. Figure 22 shows the horizontal impact responses. Only the horizontal responses and control signals are shown as the controller almost eliminates cross-coupling oscillations. The increase in damping is evident. A vertical impact shown in Fig. 23 reveals a similar performance as expected. The impact responses are fitted to a two degrees of freedom using the system identification procedure described in [21]. This allows comparison between the expected results using the model and the results obtained from experiments. The expected and obtained open loop natural frequencies $\omega_{1,ol}, \omega_{2,ol}$ and similarly closed loop natural frequencies $\omega_{1,cl}, \omega_{2,cl}$ are compared in Table 3, and show good agreement. Table 4 similarly compares the expected and obtained open loop damping factors $\zeta_{1,ol}, \zeta_{2,ol}$ and closed loop damping factors $\zeta_{1,cl}, \zeta_{2,cl}$. The results match within a factor two, which is considered a good agreement. A root locus analysis in [28], show that a small change in proportional gain results in a large change in damping factor for the gas bearing, similarly a small model uncertainty can cause a large damping factor uncertainty.

The measured impact responses are validated against the model using the following approach. An impact enters the rotor-bearing dynamics directly without the time delay and the piezoactuator dynamics, but it enters with a scaling factor g_f as the impact is a force signal $f(t)$, and the model input is a difference of piezoactuator positions. The impact response is thus given in the Laplace domain as $\mathbf{p}(s) = \mathbf{G}_b(s) g_f f(s)$ from Eq. 8. This scaling factor is found using a linear least squares on the measured and simulated non-scaled response. Figures 24 and 25 show comparisons of the measured and simulated horizontal and vertical impacts, which show great agreement.

The controller stabilises the controllable gas bearing for non-zero rotation speeds as well, which can be validated

Damping factor	$\zeta_{1,ol}$ $[-]$	$\zeta_{1,cl}$ $[-]$	$\zeta_{2,ol}$ $[-]$	$\zeta_{2,cl}$ $[-]$
Expected from model	0.035	0.318	0.029	0.424
Obtained Experimentally	0.026	0.658	0.016	0.446

Table 4: Expected and obtained open loop damping factors $\zeta_{1,ol}$, $\zeta_{2,ol}$ and expected and obtained closed loop damping factors $\zeta_{1,cl}$, $\zeta_{2,cl}$.

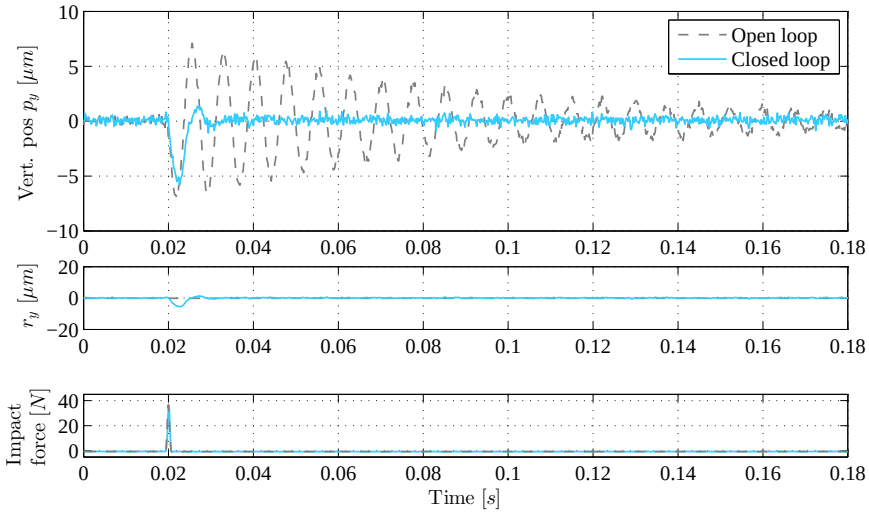

Figure 23: Vertical open and closed loop impact responses and measured impact forces.

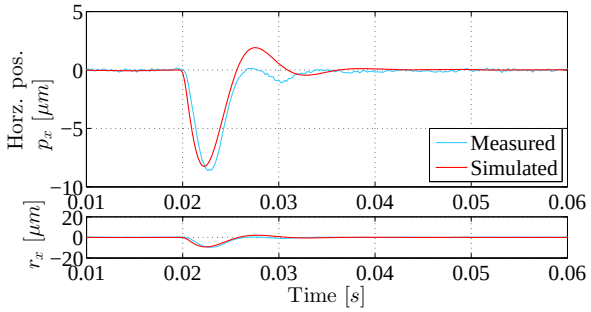

Figure 24: Simulated and measured horizontal closed loop impact response.

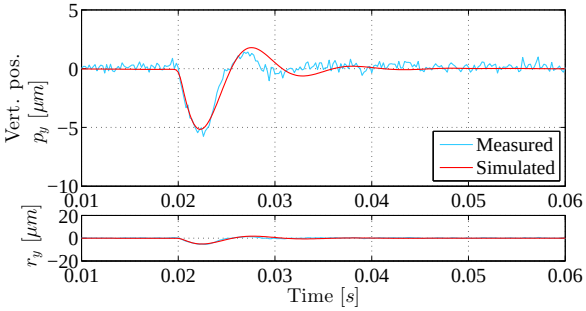

Figure 25: Simulated and measured vertical closed loop impact response.

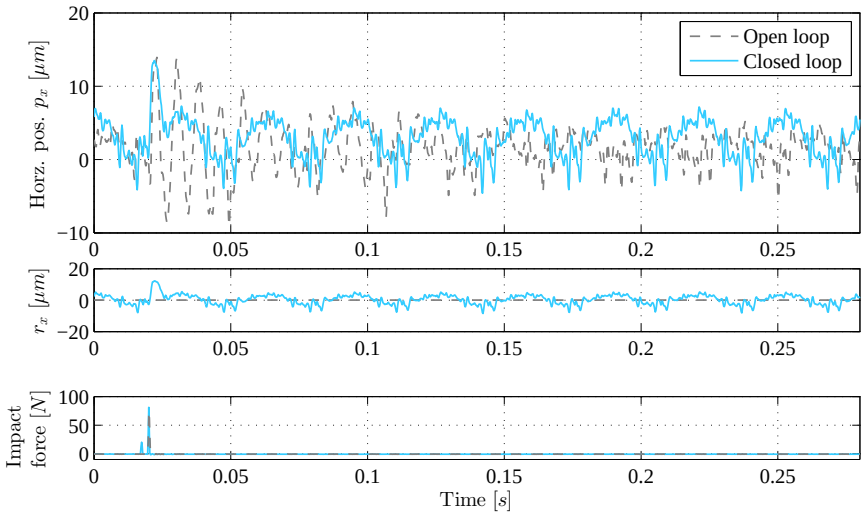

Figure 26: Experimental open vs closed loop horizontal impact response at $\bar{\Omega} = 2.05\ krpm$.

from the sensitivity function. This is proven for a rotational speed of $\bar{\Omega} = 2.05\ krpm$. Figures 26 and 27 show a horizontal and a vertical impact respectively. Here, the run-out filter has not been used to remove mass unbalance response. The mass unbalance response is more pronounced in the horizontal direction, still, the damping increase is evident.

The obtained controller performance is close to the expected. The results show, that the proposed modelling methodology can be used to develop accurate models, which can be used effectively for model based controller design.

6. Discussion

The presented approach offers a systematic procedure to models of rotor-bearing systems. The models have low complexity, yet they suffice for controller design since they capture the essential dynamics. The procedure is general in the sense that in many real applications, the mathematical model does not describe the behaviour of the plant with sufficient accuracy, which makes the model difficult to use for model based controller design. The methodology of the grey-box identification can be applied ”in situ” and accurately identifies eigenfrequencies and damping factors, which are in general difficult to estimate for eigenfrequencies so closely placed. The suggested method does not require knowledge of the geometry of the test rig to be modelled, and it avoids solving the Reynolds equation, CFD methods and finite element modelling along with the time-consuming tuning required for these methodologies. The suggested method does not allow direct estimation of the gyroscopic effect nor the mass directly, nor are they necessary for control purposes. However, their effects are implicitly included in the identified parameters. The mass matrix can be estimated from impact responses with known impact forces. The proposed filter is capable of removing both run-out and mass unbalance, and it can be applied online. This gives the possibility of using the controller to counteract mass unbalance or to only be active when the disc deviates from the mass unbalance orbit. The grey-box method imposes a parameter structure, which allows comparisons of the grey-box model parameters across identified models. This is different from black-box models, where different sets of model parameters can represent the same system. The approach has potential of being extended to other types of controllable bearings. The method is general in the sense that influence from e.g. eccentricity or other factors could have been included by performing system identification for a range of those factors.

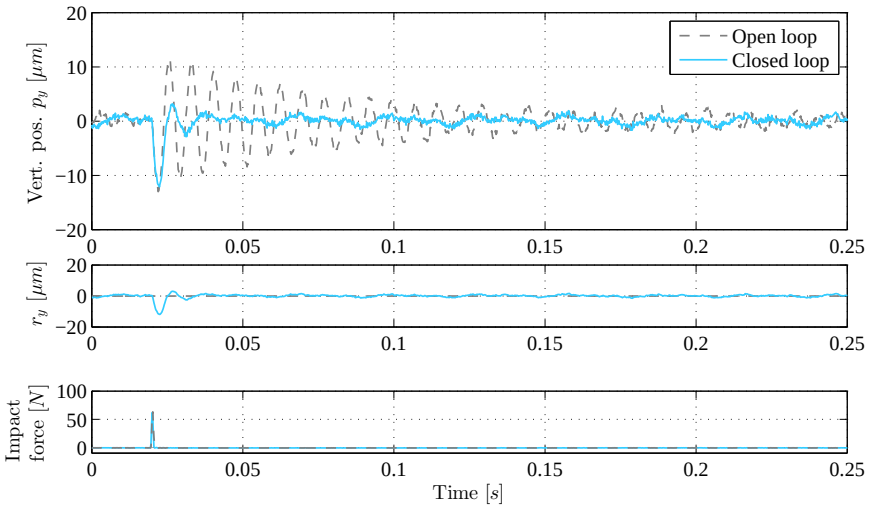

Figure 27: Experimental open vs closed loop vertical impact response at $\bar{\Omega} = 2.05\ krpm$.

7. Conclusion

Grey-box modelling was used to successfully develop accurate linear models of an entire rotor-bearing-actuator system from experimental data. The models were identified "in situ" without knowing the exact geometry of the machine to be modelled, and the developed models were shown to be suitable for controller design due to their low complexity. The model was decomposed to two subsystems: an actuator dynamics and a rotor-bearings dynamics, where the subsystems were identified separately. It was found that incorporation of the air pressure build-up dynamics was necessary to match observed behaviour, which was accomplished by approximation of the unknown time delays. The approximated delays could then be included as parameters in the grey-box identification. A filter was shown to significantly improve the lateral disc movement measurement quality by filtering out mass unbalance and run-out to allow micrometer precision measurement. The locally identified models were used to derive a linear parameter varying model describing the behaviour of the rotor-bearing system over the operating range, defined by the combination of injection pressure and rotational speed. The linear parameter varying model preserved important system characteristics in terms of eigenvalues, static gains and damping factors. The model was shown to allow design of model based decentralised controllers, which greatly improved the damping properties of the controllable gas bearing. This increase was verified experimentally both for a non-rotating and for a rotating condition. All results were compared with experiments. The very good agreement between the model and the experiments confirmed the suitability of the approach.

Acknowledgements

The Danish Ministry of Science, Innovation and Higher Education is gratefully acknowledged for the support to the FTP research project 12-127502. A thanks also goes to John D'Errico for his Matlab function `polyfitn.m`.

Appendix A. Experimental Characterisation and Control of Piezoactuators

Piezoelectric stacks have two inherent nonlinear phenomena: creep and hysteresis. The creep effect causes slow expansion of the piezo stacks by a few percent over a time scale of minutes. This is very slow compared to the time constants of the controllable gas bearing. Hysteresis causes uncertainties in the piezoactuator position, which is a challenge for modelling and control. A staircase response is collected for each piezoactuator to characterise the hysteresis: a stepwise increasing voltage is applied to a piezoactuator, followed by a stepwise decreasing voltage. Plotting the stationary piezoactuator position after each step as function of the applied input voltage reveals the open

Parameter	P_i $[m/m]$	z_1 $[rad/s]$	p_p $[rad/s]$
Piezoactuator 1	0.926	1996	101
Piezoactuator 2	0.927	1983	101
Piezoactuator 3	0.220	8349	101
Piezoactuator 4	0.640	2945	101

Table A.5: PD-controller parameters for piezoactuator controllers.

loop hysteresis curve. This is shown in Fig. A.28 for piezoactuator number four. For the same input voltage, the piezoactuator position differs up to $8.4\mu m$ depending on the input history. Due to variations in the piezo ceramics, the characteristics and hysteresis curve for each piezoactuator vary. A PD-controller is tuned experimentally for each piezoactuator to counteract these nonlinear effects. The controlled piezoactuators are capable of tracking desired reference positions $r_{p,i}$, and the control law for piezoactuator i, $i \in \{1, 2, 3, 4\}$ reads:

$$u_{p,i}(s) = P_i \frac{s + z_i}{s + p_p}(r_{p,i}(s) - y_{p,i}(s)) \tag{A.1}$$

The proportional gains P_i and zeros z_i have different values to account for the variation of characteristics in each piezo stack. The values can be found in Table A.5. A staircase response is collected for the uncontrolled and the PD-controlled piezoactuator to show the tracking capabilities of the PD-controller. Figure A.28 shows the stationary piezoactuator positions for the closed loop case, and Figure A.29 shows the open loop and PD-controlled piezoactuator staircase responses. Without control, the static gain at each step varies due to the hysteresis, and the piezoactuator slowly creeps. The PD-controller reduces both hysteresis and creep effect and the PD-controlled step responses are uniform. The three dashed step responses differ notably. The dashed closed loop responses is the last decreasing step response, and in this case the actuator reached saturation, which deteriorates the performance. The two dashed open loop responses have a noticeable smaller step size, since in these cases the piezoactuator reaches maximum expansion.

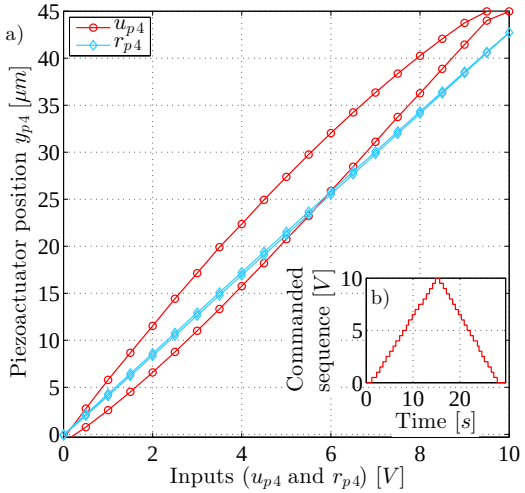

Figure A.28: a) Hysteresis curves for piezoactuator four for the open loop cases commanded the staircase sequence $u_{p,4}$ and the closed loop case commanded the position reference $r_{p,4}$. The responses are collected for a staircase input shown in b). The PD-controller efficiently eliminates the hysteresis.

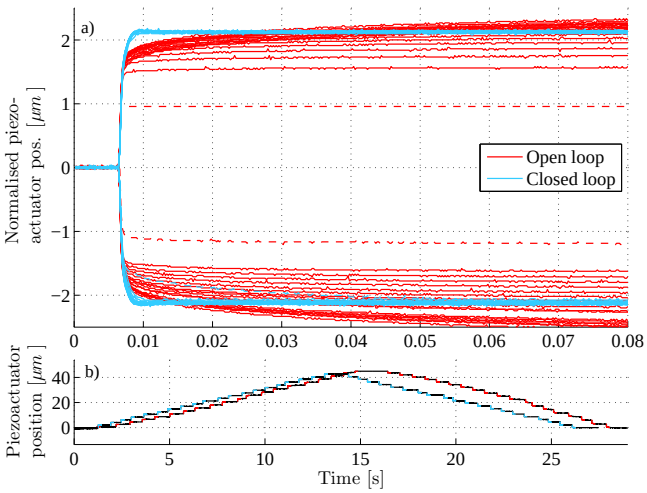

Figure A.29: Open loop and PD-controlled piezoactuator staircase responses. b) shows the piezoactuator position during the staircase response, and a) shows the individual steps, which were normalised by subtracting the offsets in time and position from each response. In the uncontrolled case, the stationary position varies due to hysteresis, and the piezoactuators creep. The PD-control reduces both hysteresis and creep effect.

Appendix B. Fitted Coefficients

Table B.6 contains the coefficients of fitted polynomials of the form Eq. 16.

Stiffness	$k_{0,ij}\left[\frac{N}{g\cdot m}\right]$	$k_{1,ij}\left[\frac{N}{g\cdot m\cdot bar}\right]$	$k_{2,ij}\left[\frac{N}{g\cdot m\cdot rpm}\right]$	$k_{3,ij}\left[\frac{N}{g\cdot m\cdot bar\cdot rpm}\right]$	$k_{4,ij}\left[\frac{N}{g\cdot m\cdot bar^2}\right]$	$k_{5,ij}\left[\frac{N}{g\cdot m\cdot rpm^2}\right]$
k_{xx}	-3.168e+08	-9.758e+07	1.790e+04	-2.192e+03	7.472e+06	-1.462e+00
k_{xy}	4.020e+07	-1.023e+07	6.391e+03	1.256e+03	4.305e+05	-9.054e-01
k_{yx}	-9.321e+05	9.624e+06	-1.428e+04	2.880e+03	-1.782e+06	3.838e-01
k_{yy}	-2.832e+08	-1.026e+08	-4.493e+02	9.310e+02	5.845e+06	-7.379e-01
Damping	$c_{0,ij}\left[\frac{N\cdot s}{g\cdot m}\right]$	$c_{1,ij}\left[\frac{N\cdot s}{g\cdot m\cdot bar}\right]$	$c_{2,ij}\left[\frac{N\cdot s}{g\cdot m\cdot rpm}\right]$	$c_{3,ij}\left[\frac{N\cdot s}{g\cdot m\cdot bar\cdot rpm}\right]$	$c_{4,ij}\left[\frac{N\cdot s}{g\cdot m\cdot bar^2}\right]$	$c_{5,ij}\left[\frac{N\cdot s}{g\cdot m\cdot rpm^2}\right]$
d_{xx}	-1.855e+05	4.036e+04	-3.329e+01	1.003e-02	-3.149e+03	5.819e-03
d_{xy}	-6.016e+03	-3.643e+03	4.422e-01	3.002e-01	7.513e-02	3.918e-04
d_{yx}	3.087e+04	-8.330e+03	-3.198e+00	-5.626e-01	4.052e-02	-3.087e-01
d_{yy}	-2.673e+05	6.863e+04	-7.541e+00	7.258e-01	-5.339e+03	6.750e-04
Input gain	$b_{0,ij}\left[\frac{N}{g\cdot m}\right]$	$b_{1,ij}\left[\frac{N}{g\cdot m\cdot bar}\right]$	$b_{2,ij}\left[\frac{N}{g\cdot m\cdot rpm}\right]$	$b_{3,ij}\left[\frac{N}{g\cdot m\cdot bar\cdot rpm}\right]$	$b_{4,ij}\left[\frac{N}{g\cdot m\cdot bar^2}\right]$	$b_{5,ij}\left[\frac{N}{g\cdot m\cdot rpm^2}\right]$
b_{xx}	1.326e+09	1.294e+07	-4.671e+03	6.982e+02	-1.400e+06	1.962e-01
b_{xy}	-1.504e+07	3.229e+06	4.720e+03	-9.969e+02	-8.013e+04	2.687e-01
b_{yx}	-5.080e+06	1.514e+06	-2.549e+03	-5.538e+01	4.262e+04	-2.298e-01
b_{yy}	1.099e+08	2.427e+07	-5.691e+02	-9.093e+01	-1.545e+06	2.269e-02
Delays	$\tau_{0,i}\,[s]$	$\tau_{1,i}\left[\frac{s}{bar}\right]$	$\tau_{2,i}\left[\frac{s}{rpm}\right]$	$\tau_{3,i}\left[\frac{s}{bar\cdot rpm}\right]$	$\tau_{4,i}\left[\frac{s}{bar^2}\right]$	$\tau_{5,i}\left[\frac{s}{rpm^2}\right]$
τ_x	1.401e-03	-2.548e-04	2.348e-09	5.497e-09	1.941e-05	-5.711e-12
τ_y	7.799e-04	-1.890e-04	3.186e-08	-3.651e-09	1.325e-05	-2.466e-12

Table B.6: Coefficients of fitted polynomials of the form Eq. 16 for the key parameter $(\cdot)_{ik}$.

References

[1] J. S. Larsen, I. F. Santos, Compliant foil journal bearings-investigation of dynamic properties, in: Proceedings of the SIRM 2013, 10th International Conference on Vibrations in Rotating Machines, 2013.

[2] J. W. Powell, A review of progress in gas lubrication, Review of Physics in Technology 1 (2) (1970) 96. doi:10.1088/0034-6683/1/2/303.

[3] S. Morosi, I. F. Santos, On the modelling of hybrid aerostatic - gas journal bearings, Institution of Mechanical Engineers. Proceedings. Part J: Journal of Engineering Tribology 225 (7) (2011) 641–653. doi:10.1177/1350650111399845.

[4] H. Heshmat, Advancements in the performance of aerodynamic foil journal bearings: high speed and load capability, Journal of Tribology.

[5] C. Dellacorte, V. Lukaszewicz, M. Valco, K. Radil, H. Heshmat, Performance and durability of high temperature foil air bearings for oil-free turbomachinery, Tribology Transactions 43 (4) (2000) 774–780.

[6] T. Kim, L. Andrés, Heavily loaded gas foil bearings: A model anchored to test data, Journal of Engineering for Gas Turbines and Power 130 (1).

[7] J. S. Larsen, A. C. Varela, I. F. Santos, Numerical and experimental investigation of bump foil mechanical behaviour, Tribology International 74 (0) (2014) 46 – 56.

[8] S. Morosi, I. F. Santos, Experimental investigations of active air bearings, in: Proceedings of ASME Turbo Expo 2012, parts a and b Edition, Vol. 7, American Society of Mechanical Engineers, 2012, pp. 901–910. doi:10.1115/GT2012-68766.

[9] H. Mizumoto, S. Arii, Y. Kami, K. Goto, T. Yamamoto, M. Kawamoto, Active inherent restrictor for air-bearing spindles, Precision Engineering 19 (2-3) (1996) 141–147.

[10] A. A. Goncalves Siqueira, R. Nicoletti, N. Norrick, K. L. Cavalca, H. F. de Castro, J. Bauer, F. Dohnal, Linear parameter varying control design for rotating systems supported by journal bearings, Journal of Sound and Vibration 331 (10) (2012) 2220–2232.

[11] L. San Andrés, K. Ryu, Hybrid gas bearings with controlled supply pressure to eliminate rotor vibrations while crossing system critical speeds, Journal of Engineering for Gas Turbines and Power.

[12] G. Goodwin, S. Graebe, M. Salgado, Control System Design, Prentice Hall, 2001.
URL https://books.google.dk/books?id=7dNSAAAAMAAJ

[13] R. Herzog, M. Mohler, C. Gähler, Multivariable identification of active magnetic bearing systems, JSME International Journal, Series C: Mechanical Systems, Machine Elements and Manufacturing 40 (4) (1997) 584–592.

[14] S. Srinivasan, Y. M. Cho, Modeling and system identification of active magnetic bearing systems, in: Control Applications, 1995., Proceedings of the 4th IEEE Conference on, 1995, pp. 252–260.

[15] N.-C. Tsai, C.-H. Kuo, R.-M. Lee, Regulation on radial position deviation for vertical amb systems, Mechanical Systems and Signal Processing 21 (7) (2007) 2777–2793. doi:10.1016/i.ymssp.2007.03.005.

[16] R. Mohd-Mokhtar, L. Wang, System identification of mimo magnetic bearing via continuous time and frequency response data, in: Mechatronics, 2005. ICM '05. IEEE International Conference on, 2005, pp. 191–196. doi:10.1109/ICMECH.2005.1529251.

[17] Z. Sun, Y. He, J. Zhao, Z. Shi, L. Zhao, S. Yu, Identification of active magnetic bearing system with a flexible rotor, Mechanical Systems and Signal Processing 49 (1-2) (2014) 302–316. doi:10.1016/j.ymssp.2014.05.004.

[18] H. M. N. K. Balini, I. Houtzager, J. Witte, C. W. Scherer, Subspace identification and robust control of an amb system, Proceedings of the 2010 American Control Conference, Acc 2010, Proc. Am. Control Conf., Acc (2010) 2200–2205.
[19] N. Gibson, G. Buckner, Real-time adaptive control of active magnetic bearings using linear parameter varying models, in: SoutheastCon, 2002. Proceedings IEEE, 2002, pp. 268–272. doi:10.1109/.2002.995603.
[20] H. Ahn, S. Lee, S. Lee, D. Han, Frequency domain control-relevant identification of mimo amb rigid rotor, AUTOMATICA 39 (2) (2003) 299–307.
[21] L. R. S. Theisen, F. G. Pierart Vásquez, H. H. Niemann, I. F. Santos, M. Blanke, Experimental grey box model identification of an active gas bearing, Vibration Engineering and Technology of Machinery (2014) 963–976doi:10.1007/978-3-319-09918-7_85.
[22] S. Morosi, I. F. Santos, Active lubrication applied to radial gas journal bearings. Part 1: Modeling, Tribology International 44 (12) (2011) 1949–1958. doi:10.1016/j.triboint.2011.08.007.
[23] S. Morosi, I. F. Santos, From hybrid to actively-controlled gas lubricated bearings theory and experiment, Ph.D. thesis, Technical University of Denmark (2011).
[24] K. Leang, S. Devasia, Iterative feedforward compensation of hysteresis in piezo positioners, 42nd IEEE Conference on Decision and Control, vols 1-6, Proceedings (2003) 2626–2631.
[25] H. Janocha, K. Kuhnen, Real-time compensation of hysteresis and creep in piezoelectric actuators, Sensors and Actuators, A: Physical 79 (2) (2000) 83–89, cited By 102. doi:10.1016/S0924-4247(99)00215-0.
[26] L. Ljung, System identification - Theory for the User, Prentice-Hall, 1999.
[27] W. Cummins, The impulse response function and ship motion,technical report 1661, Tech. rep., David Taylor Model Basin - DTNSRDC (1962).
URL http://marinecontrol.org/References/papers/Cummins%201962.pdf
[28] L. R. S. Theisen, R. Galeazzi, H. H. Niemann, I. F. Santos, Experimental investigations of decentralised control design for the stabilisation of rotor-gas bearings, 2015.
[29] Freudenberg, Looze, Right half plane poles and zeros and design tradeoffs in feedback systems, IEEE Transactions on Automatic Control 30 (6) (1985) 555–565. doi:10.1109/TAC.1985.1104004.

List of Figures

1 The experimental controllable gas bearing setup. A turbine (1) drives a flexible shaft (2), which is supported by both a ball bearing (3) and the controllable gas bearing (4) with four piezoactuated injectors. A disc (5) is mounted in one end to preload the journal and displacement sensors (6) measure the lateral movement of the disc in the shown reference frame. A quadrature encoder (7) measures the angular position. . . . 3

2 CAD drawing of the test rig: a) the test rig with the controllable gas bearing cut in half. Major dimensions are included in millimetre [mm]. b) zoom of a piezoactuator. The piezo electric stack pushes a pin, which controls the injector opening. c) zoom of the injector pin and journal. . . . 4

3 The piezoactuators are controlled pairwise using a differential principle. A reference signal r_x is sent to the pair of piezoactuators mounted horizontally, and a reference signal r_y is sent to the pair mounted vertically. . . . 4

4 Overview of the system identification process. A perturbation of the commanded piezoactuator positions perturbs both the piezoactuators and the shaft and disc. An actuator model can the be identified from the $\{\mathbf{r}, \mathbf{u}\}$ data sets, and a rotor-bearing model from the $\{\mathbf{u}, \mathbf{p}\}$ data sets. . . . 5

5 Steady state characterization of input-output gains at $\bar{P}_{\text{inj}} = 6bar$, $\bar{\Omega} = 0rpm$: the experimental data reveal a linear mapping from $\mathbf{u}$ to lateral disc position $\mathbf{p}$. . . . 6

6 Overview of the rotor-bearing model: the difference of piezoactuator positions $\mathbf{u}$ enters as input into the Padé approximated delays modelling the fluid memory effect. The signal $\mathbf{d}_b$ models the differences between measured and model response including measurement noise. . . . 8

7 Example of identification from data set collected at $\bar{P}_{\text{inj}} = 5bar, \bar{\Omega} = 6.0krpm$, here a zoom in time interval in the interval $t \in [1.2 : 1.4]s$. The piezoactuator positions $[u_x, u_y]$ shown in c) cause disc vibrations. The lateral disc movement $\mathbf{p}_{meas} = [p_x, p_y]$ and the simulated movement using the identified model $\mathbf{p}_{pred} = [\hat{p}_x, \hat{p}_y]$ subject to same excitation is shown in a) and b). The model predicts both the direct and the cross coupling oscillations. . . . 9

8 Estimated gains $\kappa_{a,x}, \kappa_{a,y}$, slow poles $p_{1,x}, p_{1,y}$, and fast poles $p_{2,x}, p_{2,y}$ of the actuator models from Eq. 12 across the models identified from different data sets. . . . 10

9 Cross-validation fit percentages of the horizontal and vertical residuals in validation of the identified bearing submodels cross-validated on other data sets. . . . 11

10 Horizontal and vertical validation fit percentages of the identified actuator submodels cross-validated on other data sets. . . . 11

11 Identified stiffness coefficients as function of injection pressure P_{inj} ($1bar = 0.1MPa$) and rotational speed Ω, along with 2^{nd} order polynomial fit, assisting lines indicate 3D location of the parameter estimates. . . . 12

12 Identified damping coefficients as function of injection pressure P_{inj} ($1bar = 0.1MPa$) and rotational speed Ω, along with 2^{nd} order polynomial fit, assisting lines indicate 3D location of the parameter estimates. . . . 12

13 Identified input gain coefficients as function of injection pressure P_{inj} ($1bar = 0.1MPa$) and rotational speed Ω, along with 2^{nd} order polynomial fit, assisting lines indicate 3D location of the parameter estimates. . . . 13

14 Identified and linear parameter varying model horizontal time delay [$samples@5kHz$] between Eq. 17 over varying speed and injection pressure, ($1bar = 0.1MPa$). . . . 13

15 Identified and linear parameter varying model vertical time delay [$samples@5kHz$] between Eq. 17 over varying speed and injection pressure. . . . 13

16 Natural frequencies of the experimentally identified models and the linear parameter varying model Eq. 17 over varying speed and injection pressure, ($1bar = 0.1MPa$). . . . 15

17 Damping factors of experimentally identified models and the linear parameter varying model Eq. 17 over varying speed and injection pressure, ($1bar = 0.1MPa$). . . . 15

18 Comparison of static gains between experimentally identified models and the linear parameter varying model Eq. 17 over varying speed and injection pressure. . . . 16

19 Block diagram of the closed loop system. The horizontal piezoactuators are decoupled from the vertical ones. The lateral disc movement is used by the feedback controller to generate piezoactuator reference positions. 16
20 Output sensitivity $\mathbf{S}_o$ and closed loop controller sensitivity $\mathbf{K}_{pl}\mathbf{S}_o$ for the controller $\mathbf{K}_{pl}$. 17
21 Bode magnitude diagram for the open loop system $\mathbf{G}$ and closed input disturbance response $\mathbf{S}_o\mathbf{G}$ for the controller $\mathbf{K}_{pl}$. 17
22 Horizontal open and closed loop impact responses and measured impact forces. 18
23 Vertical open and closed loop impact responses and measured impact forces. 19
24 Simulated and measured horizontal closed loop impact response. 19
25 Simulated and measured vertical closed loop impact response. 19
26 Experimental open vs closed loop horizontal impact response at $\bar{\Omega} = 2.05\ krpm$. 20
27 Experimental open vs closed loop vertical impact response at $\bar{\Omega} = 2.05\ krpm$. 21
A.28 a) Hysteresis curves for piezoactuator four for the open loop cases commanded the staircase sequence $u_{p,4}$ and the closed loop case commanded the position reference $r_{p,4}$. The responses are collected for a staircase input shown in b). The PD-controller efficiently eliminates the hysteresis. 22
A.29 Open loop and PD-controlled piezoactuator staircase responses. b) shows the piezoactuator position during the staircase response, and a) shows the individual steps, which were normalised by subtracting the offsets in time and position from each response. In the uncontrolled case, the stationary position varies due to hysteresis, and the piezoactuators creep. The PD-control reduces both hysteresis and creep effect. 22